Institut für Ionenstrahlphysik und Materialforschung

Helmholtz-Zentrum Dresden-Rossendorf

Highly Mismatched $GaAs_{1-x}N_x$ and $Ge_{1-x}Sn_x$ Alloys Prepared by Ion Implantation and Ultrashort Annealing

Dissertation

zur Erlangung des akademischen Grades

Doctor rerum naturalium (Dr. rer. nat.)

vorgelegt der Fakultät Mathematik und Naturwissenschaften

der Technischen Universität Dresden

von

Kun Gao

geboren am 19.01.1986 in China

Eingereicht am 29.09.2014

Verteidigt am 19.12.2014

Gutachter

Prof. Dr. Manfred Helm

Prof. Dr. Georgeta Salvan

ACKNOWLEDGEMENTS

On September 8th, 2011, I arrived in Germany and started my PhD study at Helmholtz-Zentrum Dresden-Rossendorf. Now three years have passed, and my study as a PhD student is coming to an end. I am sitting at my desk, trying to recall all those moments I'm grateful for and all the people I would like to thank for supporting me along this journey.

First and foremost, I would like to thank my supervisor, Prof. Manfred Helm, for his suggestions during my study and for his critical discussions and comments on my work, which contributed a lot to my scientific growth.

I would like to express my sincere gratitude to Dr. Shengqiang Zhou. As our team leader and my co-supervisor, Shengqiang has helped me so much from many aspects. I could not have survived throughout my project without his invaluable encouragement, support, and guidance.

I am also very grateful to Dr. Slawomir Prucnal for his constant help with my research. Slawek is quite knowledgeable with my topic. I can always get inspiring ideas from the discussion with him.

I would like to thank Dr. Wolfgang Skorupa for his comments and suggestions on my work. Under his leadership, the group of FWIM is in a friendly and flexible working atmosphere.

I'm very thankful to Dr. Carsten Baethz and Dr. Olga Roshchupkina for their help with synchrotron XRD measurements, as well as Dr. Rene Huebner and Ms. Elfi Christalle for the TEM and SEM measurements. I thank the FWIZ group for all the ion implantation work for me. The help with FTIR test from Carsten Franke, the help with RBS test from Richard Wilhelm and Rene Heller, the help with transmittance test from Steffen Cornelius, and the help with flash lamp annealing from Thomas Schumann, are also greatly appreciated.

I greatly appreciate the continuous support from Prof. Jiada Wu, my supervisor in my master's study. The suggestions and comments from him are

always helpful. The work of sample preparation from his group also contributes to my current research at HZDR.

Additional thanks are due to Yutian Wang, Ye Yuan, Muhammad Khalid, Xin Ou, Menglei Xu, Fang Liu, Hendrik Hentschel, and Lars Rebohle, for their help with my work in many aspects. I also thank Yao Shuai, Wenbo Luo, Chuangui Wu, Yu Liu, Anna Semisalova, Gerard Larkin, and all the other FWIMers. Together we create a great group. Thanks to Yanda Ji, Lingen Huang, Wen Feng, and all the other Chinese friends in HZDR and in Dresden. Life is more colorful with them.

I thank all my Chinese classmates who have been keeping in touch with me. May our friendship last forever.

Finally, I want to extend my deepest gratitude to my parents and other family members. I am greatly thankful for the education and support from them throughout my growth, which makes me who I am.

Gao, Kun 高昆

September 8th, 2014

ABSTRACT

Doping allows us to modify semiconductor materials for desired properties such as conductivity, bandgap, and / or lattice parameter. A small portion replacement of the highly mismatched isoelectronic dopants with the host atoms of a semiconductor can result in drastic variation of its structural, optical, and / or electronic properties. Here, the term "mismatch" describes the properties of atom size, ionicity, and / or electronegativity. This thesis presents the fabrication of two kinds of highly mismatched semiconductor alloys, i.e., $Ge_{1-x}Sn_x$ and $GaAs_{1-x}N_x$. The structural and optical properties of the prepared $Ge_{1-x}Sn_x$ and $GaAs_{1-x}N_x$ have been investigated. The results suggest an efficient above-solubility doping induced by non-equilibrium methods of ion implantation and ultrashort annealing. Pulsed laser melting promotes the regrowth of monocrystalline $Ge_{1-x}Sn_x$, whereas flash lamp annealing brings about the formation of high quality $GaAs_{1-x}N_x$ with room temperature photoluminescence. The bandgap modification of $Ge_{1-x}Sn_x$ and $GaAs_{1-x}N_x$ has been verified by optical measurements of spectroscopic ellipsometry and photoluminescence, respectively. In addition, effective defect engineering in GaAs has been achieved by flash lamp annealing, by which a quasi-temperature-stable photoluminescence at 1.3 μm has been obtained.

KURZFASSUNG

Dotierung ermöglicht es, die Eigenschaften von Halbleitermaterialien, wie Leitfähigkeit, aber auch Bandabstand und / oder Gitterkonstanten gezielt zu verändern. Wenn ein Halbleiter mit einer kleinen Menge unterschiedliche Fremdatome dotiert wird, kann dies in einer drastischen Modifikation der strukturellen, optischen und / oder elektronischen Eigenschaften resultieren. Der Begriff "unterschiedlich" bedeutet hier die Eigenschaften von Atomgröße, Ioniztät und / oder Elektronegativität. Diese Doktorarbeit beschreibt die Herstellung von zwei Arten von stark fehlangepassten Halbleiterlegierungen: $Ge_{1-x}Sn_x$ und $GaAs_{1-x}N_x$. Die strukturellen und optischen Eigenschaften von $Ge_{1-x}Sn_x$ und $GaAs_{1-x}N_x$ wurden untersucht. Die Ergebnisse deuten auf eine effiziente Dotierung oberhalb der Löslichkeit, induziert durch die Nicht-Gleichgewichtsverfahren Ionenimplantation und Ultrakurzzeit-Ausheilung. Gepulstes Laserschmelzen ermöglicht das Nachwachsen von monokristallinem $Ge_{1-x}Sn_x$, während die Blitzlampenausheilung in der Bildung von $GaAs_{1-x}N_x$ hoher Qualität mit Photolumineszenz bei Raumtemperatur resultiert. Die Änderung der Bandlücke von $Ge_{1-x}Sn_x$ und $GaAs_{1-x}N_x$ wurde durch die optischen Methoden der spektroskopischen Ellipsometrie und Photolumineszenz verifiziert. Darüber hinaus konnte in ausgeheiltem $GaAs_{1-x}N_x$ eine quasi-temperaturstabile Photolumineszenz bei 1,3 µm beobachtet werden.

CONTENTS

Chapter 1 Introduction

1.1 Highly mismatched semiconductor alloys (HMAs)

Doping is an efficient method to modify semiconductor materials for desired properties such as bandgaps and / or lattice parameters. Common doped semiconductors can be considered as compounds of several kinds of semiconductors which are isostructural and composed of isovalent elements with relatively matched properties in view of atom size, electronegativity, and / or ionicity, etc. i.e., lightly mismatched semiconductor alloys (LMAs) [1]. In most cases, these compounds can easily dissolve in each other, hence forming semiconductor alloys with a large variety of compositions. Studies on the synthesis and characterization of such kind of materials, e.g., SiGe, InGaAs, InGaAsP, and InGaN, have been massively performed with different compositions. The fabrication techniques (e.g., molecular beam epitaxy (MBE), metalorganic chemical vapor deposition (MOCVD)) have also been well developed.

According to the Vegard's law and the extensional virtual crystal approximation (VCA), the structural [1], electronic [2,3], and optical properties [3-5] of those common LMAs can be approximated by a linear interpolation between the end point materials. The deviation of the experimental data from the linear approximation is relatively small, and can be compensated by a quadratic bowing parameter [1]. For instance, the expected lattice parameter d [1] and the bandgap E_g [4] of an alloy $A_xB_{(1-x)}$ can be expressed as follows:

$$d(x) = xd(A)+(1-x)d(B)+b_1x(1-x),$$

$$E_g(x) = xE_g(A)+(1-x)E_g(B)+b_2x(1-x),$$

where A and B represent the two end point materials, x is the stoichiometric fraction, b_1 and b_2 are the bowing parameter for lattice parameter and the bandgap, respectively.

Highly mismatched semiconductor alloys (HMAs) are a group of semiconductor alloys in which the host atoms are partially replaced by some isoelectronic impurities with very dissimilar properties such as ionization energy and / or electronegativity. Due to these distinct differences, a small amount of dopant is able to introduce considerable changes to the properties of the host material. In recent years, theoretical and experimental studies on HMAs (e.g., $GaAs_{1-x}N_x$, $GaP_{1-x}N_x$, and $Ge_{1-x}Sn_x$) have been extensively conducted for their interesting and distinct optoelectronic properties [1-9].

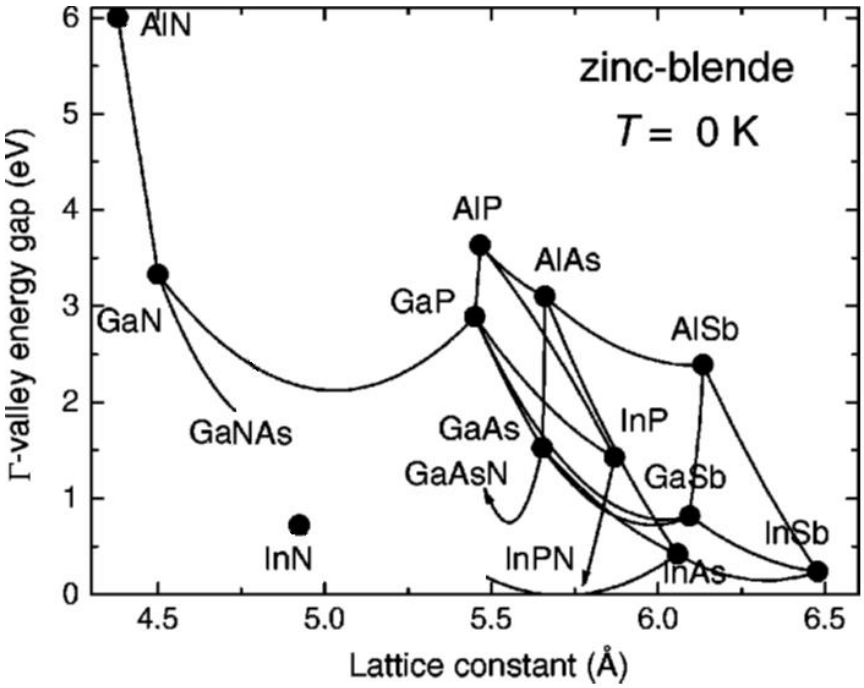

Figure 1.1 Direct bandgap energies of III-V compounds with respect to lattice parameter. Direct Γ-valley energy gap as a function of lattice constant for the zinc blende form of 12 III–V binary compound semiconductors (points) and some of their random ternary alloys (curves) at temperature of 0 K. The energy gaps for certain ternaries such as AlAsP, InAsN, GaAsN, InPN, and GaPN are extended into regions where no experimental data have been reported. For GaAsN and InPN, the arrows indicate the boundaries of the regions where the gap dependence on composition may be predicted with any accuracy. Adapted from ref. [5].

The variations of the properties for HMAs are far from linear behavior. The HMAs exhibit an enormous bandgap bowing and subsequent other properties (i.e., a much larger bowing parameter than LMAs). From one end composition to the other, the bandgap first shows a giant decrease before increasing finally to the bandgap of the other end member [1,5]. The $GaAs_{1-x}N_x$ system provides a typical example of the significant bandgap energy bowing due to the large mismatch in atomic radius and electronegativity between the two anion elements. Figure 1.1 shows the bandgap and lattice variations for the common III-V semiconductors [4]. On the contrary of the quasi-linear dependence of other materials, a striking feature is the substantial decrease of bandgap of GaAs with N-doping. This abnormal behavior has been extensively studied both theoretically and experimentally [5,8,10]. Band anti-crossing (BAC) model was introduced to explain such phenomena in $GaAs_{1-x}N_x$ and $GaP_{1-x}N_x$ systems [8,11], and then was also applied for other III-V and II-VI HMAs such as $GaSb_{1-x}As_x$, $ZnSe_{1-x}O_x$, and $CdTe_{1-x}O_x$ systems [8,12-14].

Epitaxial thin films are the mostly used media in microelectronic and optoelectronic devices. In most cases, epitaxial layers should be prepared on a certain crystalline substrate which is relatively uncomplicated for bulk growth. For the mass production of semiconductors in industry, a high degree of crystallinity is an essential consideration, as the defects in the materials can be a critical draw-back of the devices. It has been known that defects can reduce the conductivity dramatically in microelectronic materials and quench the luminescence in optoelectronic materials. Therefore, monocrystalline structures are preferred in most semiconductor devices. However, it is challenging to grow most of the semiconductors as high quality bulk materials, and nearly impossible to grow bulk single crystal alloys with adequately-controlled chemistry [1]. Secondly, the high cost and low efficiency due to the complexity of growth are also a concern for the growth of many bulk

materials. Moreover, the demand of integration with Si-based IC technologies also requires well developed thin film deposition techniques for semiconductor alloys. To avoid defects, the crystal structure and the lattice parameter of the fabricated layer should be as close as possible to the substrate. Considering the limited category of bulk substrates as a significant constraint, the functional layer must be designed for both optoelectronic properties and structural properties such as crystal structure and lattice parameter. This can usually be accomplished but it adds significant complexity to the process. Even though common lightly mismatched semiconductor alloys can be designed for a certain bandgap, the lattice parameter will also be influenced by the high concentration alloying. On the contrary, considerable band structure changes can be made by a small amount of doping in HMAs. This feature affords us the possibility of preparing semiconductors with desired electronic and optical properties in the meantime similar crystalline structural properties can be kept as the host material. Taking GaAs based alloys as an example, about 12 at. % of slightly mismatched In substituting Ga can bring about a decrease of the direct bandgap of GaAs by 170 meV, whereas in the case of highly mismatched N substituting As, only 1 at. % is needed [15]. In the two cases, the lattice variations would be about 1% expansion for In-doping, and only 0.2% shrinkage for N-doping, respectively. Therefore, the application of HMAs can broaden the scope of semiconductors (the range of our choices for semiconductors). However, due to the huge divergence between the host species and the dopant species mentioned above, the solid solubility limit of the different compositions of HMAs is normally very low, which is predicted by the Hume-Rothery rules [16]. Therefore, it is challenging to synthesize HMAs compared with those lightly mismatched alloys listed above. For the past few years, many groups have made great advances in MBE growth of HMAs, e.g., GaAsN [17] and GeSn [18] alloys under non-equilibrium conditions. On the

other hand, the growth of HMAs by MOCVD or sputtering, both of which are compatible for mass production, is in most cases still immature.

1.2 The aim and structure of this thesis

As discussed above, the applications of HMAs can broaden the scope of semiconductors materials thereby affording us more possibilities for device design. The aim of this thesis is to discuss the preparation of two kinds of HMAs (i.e., dilute nitride $GaAs_{1-x}N_x$ alloys and germanium tin $Ge_{1-x}Sn_x$ alloys) by ion implantation and ultra-short thermal treatment (i.e., flash lamp annealing (FLA) and pulsed laser melting (PLM)), which are applicable for semiconductor mass production and compatible with Si-based IC-industry. The obtained HMAs have been characterized for structural and optical properties.

Ion implantation is an efficient doping technique for the process and modification of semiconductors by which the dopant ions are accelerated by an electric field and then impact into the host material. The impacted ions will be stopped as a consequence of collisions with host atoms. The depth distribution of the implanted dopant can be calculated by SRIM code [19]. Since ion implantation is a non-equilibrium process, the doping beyond solubility is achievable. The main drawback of ion implantation is the amorphization of the implanted layer due to the high energy impact of the implanted ions. Annealing is applied to recrystallize the lattice of the implanted region and to incorporate the dopants into the lattice sites. Due to strong diffusion and / or segregation of dopants appearing during long term annealing, the conventional furnace annealing is not applicable. Flash lamp annealing (FLA) [20,21] and pulsed laser melting (PLM) [22] are the two ultra-short annealing techniques discussed in this thesis as substitutions of furnace annealing and rapid thermal annealing.

The main challenge for the preparation of HMAs is to overcome the low solid solubility limit of the implanted dopants and to incorporate them into the host materials. To confirm the achievement of our objectives, various kinds of structural and optical characterization was performed.

Within the topic of HMAs, this thesis is organized as follows:

In Chapter 2, the history and the present research status of the materials discussed in this thesis are reviewed.

In chapter 3, the experimental techniques used in sample preparation, i.e., ion implantation, pulsed laser melting, and flash lamp annealing, are briefly introduced.

In Chapter 4, we present our work on $Ge_{1-x}Sn_x$ alloys. Different Sn-implantation fluences and post-implantation PLM conditions were applied to alloy Ge with Sn. Monocrystalline $Ge_{1-x}Sn_x$ alloys have been prepared through a nanoseconds range liquid phase epitaxial process.

In Chapter 5, synthesis and characterization of dilute nitride $GaAs_{1-x}N_x$ are presented. Different from the formation of $Ge_{1-x}Sn_x$ alloys, the regrowth of $GaAs_{1-x}N_x$ is controlled in a solid phase recrystallization process by FLA to avoid the generation of numerous kinds of defects. Our investigation confirms the room-temperature photoluminescence from $GaAs_{1-x}N_x$ layer, which indicates a low concentration of defects from the FLA-induced $GaAs_{1-x}N_x$ layer.

In Chapter 6, temperature-stable 1.3 μm emission from GaAs based on defect-engineering are presented. First we have observed the 1.3 μm emission from FLA-prepared $GaAs_{1-x}N_x$. Further investigation was conducted to reveal the origin and to enhance the 1.3 μm emission. According to our analysis, this emission is based on the transition from arsenic vacancy to X-level [23]. In addition, an enhancement of the 1.3 μm PL emission by two-orders of magnitude has been achieved by indium-doping.

In Chapter 7, all the results are summarized. An outlook of the future work on HMAs prepared by ion implantation and ultrashort annealing are discussed.

Chapter 2 Fundamentals

2.1 Germanium tin ($Ge_{1-x}Sn_x$) alloys

Group IV semiconductor alloys have drawn substantial attention for their potential applications in optoelectronic devices capable of integration with the existing silicon based IC industry. In recent years, germanium based materials are becoming increasingly vital in Si-based photonics.

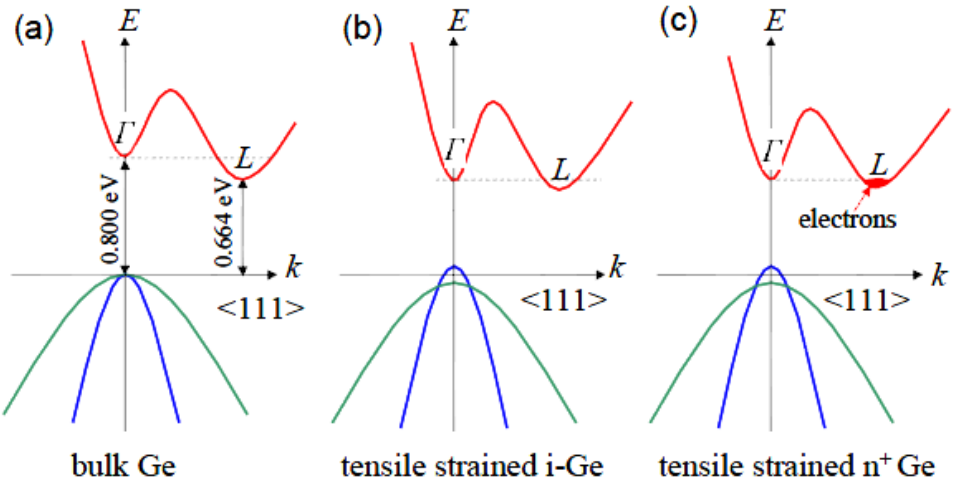

Figure 2.1.1 Schematic view of (a) direct and indirect bandgap of Ge, (b) the strain induced bandgap shrinkage of Ge, and (c) the n-type doping induced direct bandgap transition. From ref. [24].

Germanium exhibits a pseudo-direct bandgap behavior because the energy difference between its direct (Γ band minimum to valence band maximum) and indirect (L band minimum to valence band maximum) transition is only 136 meV, as shown in Figure2.1.1 (a) [24,25]. Therefore germanium can be relatively easily transformed from indirect to direct bandgap by several approaches.

By n-type doping, the L band valley can be populated by electrons until the Fermi level for the electrons is higher than the Γ band minimum. In this case,

some of the electrons whose energy is higher than the Fermi level have to populate the Γ band valley and then can recombine with holes in the valence band maximum via a direct transition [26]. This idea has been suggested by Adams and Landsberg in 1968 [27].

Yasuhiko Ishikawa *et al.* [28] have successfully reduced the difference between Γ band valley and L band valley by applying tensile strain to Ge layer. The difference can be reduced to 115 meV by 0.25% tensile strain. According to the deformation potential theory [29], the difference can be completely compensated by 2% tensile strain.

Jifeng Liu *et al.* have applied an n-type doping to a tensile strained Ge layer to fill the L band valley until the Fermi level is higher than the Γ band minimum, thus realize a direct bandgap transition [24]. Figure 2.1.1 gives a schematic view of the strain induced bandgap shrinkage (b) and the n-type doping induced direct bandgap transition (c).

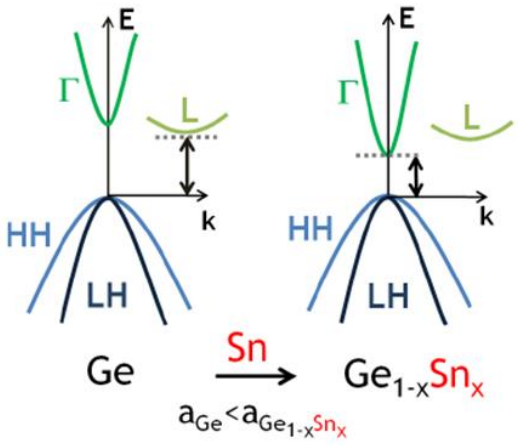

Figure 2.1.2 Schematic diagram of $Ge_{1-x}Sn_x$ band structure variation. From ref. [30].

On the other hand, Sn-alloying with Ge has also been studied to achieve a direct bandgap for Ge-based semiconductor. Considering the fact that Sn-alloying will increase the lattice parameter of Ge, both energy levels of the Γ and L bands will be reduced. According to the analysis based on BAC model

by K. Alberi *et al.* [31], the Γ band minimum will decrease faster than the L band minimum with increasing Sn composition. The regime is shown schematically in Figure 2.1.2. As the most promising tunable direct bandgap material among all group-IV materials, $Ge_{1-x}Sn_x$ has been studied comprehensively in recent years. Monocrystalline $Ge_{1-x}Sn_x$ alloys have been predicted to convert from indirect to direct bandgap semiconductor with a Sn concentration of above 6% through *ab initio* calculations [26,32,33]. By applying the valence band anticrossing model, K. Alberi *et al.* have calculated the indirect-direct transition at x=0.11 for $Ge_{1-x}Sn_x$ [31]. G. He and H.A. Atwater have observed the direct transition in $Ge_{1-x}Sn_x$ alloy for x=0.12 by optical absorption measurements [34]. V.R. D'Costa *et al.* determined the direct bandgap from experiments, then calculated the concentration for the indirect to direct transition should be less than x=0.11 based on the upper limit of the computed bowing parameter (b_{ind}=1.23 eV) of indirect bandgap (see Figure 2.1.3). R. Chen *et al.* have reported the indirect-direct bandgap transition of MBE-grown unstrained $Ge_{1-x}Sn_x$ at x=0.071 [35].

In addition, there is no contradiction between the methods of achieving direct bandgap germanium stated above (i.e., via tensile strain, n-type doping, and/or via Sn-alloying), which means one can combine these methods to achieve a more realizable approach to direct bandgap $Ge_{1-x}Sn_x$ alloys. J. Mathews *et al.* have calculated the energy difference between the Γ and L bands with respect to the tensile strain and Sn-composition [33], as shown in Figure 2.1.3. According to this figure, an increase of 1% of Sn alloying in Ge is roughly equivalent to a 0.35% increase of tensile strain.

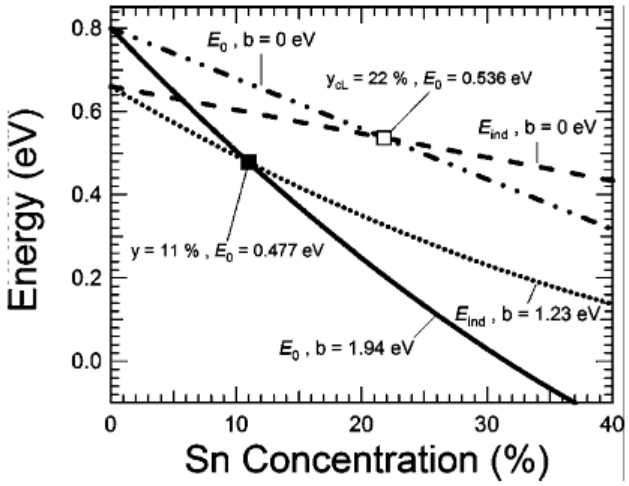

Figure 2.1.3 Predicted direct and indirect bandgap shrinkage with respect to Sn concentration (here marked as y) variation. The dash-double-dotted and dashed lines represent linear interpolations between Ge and α-Sn, respectively. The solid line is the experimental result for the direct bandgap. The dotted line represents the indirect bandgap computed with b_{ind}=1.23 eV, which is believed as an upper limit for the value of the bowing parameter. This means that the concentration for the indirect to direct transition in GeSn alloys should be less than y=0.11. From ref. [36].

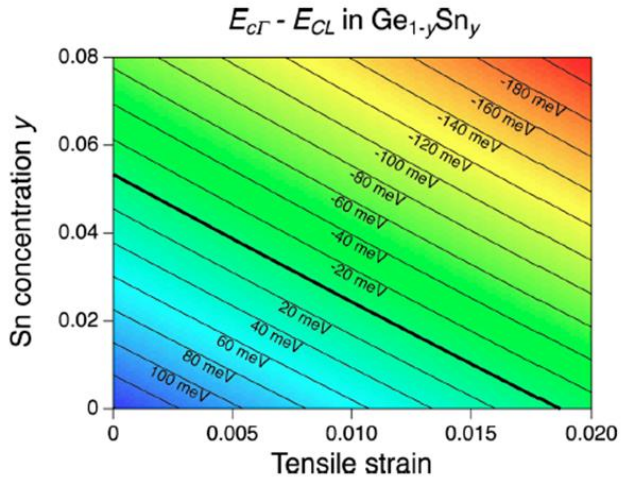

Figure2.1.4 Energy separation between the conduction band minima of the Γ band and the L band of the Brillouin zone in the $Ge_{1-x}Sn_x$ alloys. The tensile strain is biaxial in the (001) plane. The thick line indicates the direct-indirect crossover. From ref. [32,33,37].

In the meantime, the $Ge_{1-x}Sn_x$ alloys are also attractive for electronic and optical applications in virtue of the predicted high carrier mobility [38,39]. Moreover, Ge and Si have similar structural properties and can easily be alloyed with each other in any proportion. Based on these facts, the $Ge_{1-x}Sn_x$ system is promising for the realization of direct-gap semiconductor optoelectronic devices fully integrated with Si technology [40].

However, it is challenging to achieve $Ge_{1-x}Sn_x$ alloys with high Sn composition due to the very low solid solubility (<1%) of Sn in Ge and the lattice mismatch between Sn and Ge of 14.7% [41,42]. Different methods (e.g., molecular beam epitaxy (MBE) [18,31,43], chemical vapor deposition (CVD) [33,44], rf magnetron sputtering [39], pulsed laser induced epitaxy [41,45,46]) have been applied to synthesize $Ge_{1-x}Sn_x$ alloys with different Sn composition. CVD growth of $Si_yGe_{1-x-y}Sn_x$ has been achieved by V.R. D'Costa *et al.*, the idea of which is to compensate the lattice mismatch between $Ge_{1-x}Sn_x$ and Ge. Later H. Lin *et al.* have synthesized $Si_yGe_{1-x-y}Sn_x$ by MBE with an InGaAs buffer layer on the GaAs substrate. This opens up new possibilities to achieve bandgap modification with a constant lattice parameter [44].

In Chapter 4, we present the low temperature synthesis of $Ge_{1-x}Sn_x$ alloy on Ge wafer by ion implantation and PLM. Ion implantation is an efficient non equilibrium doping method and is a standard processing technique in Si based IC industry. By ion implantation it is possible to inject Sn dopants into Ge beyond its solid solubility limit. The amorphization due to ion implantation can be overcome by post-implantation thermal treatment. Ultra-short pulsed laser irradiation melts only the surface layer (less than 200 nm) including the whole implanted part whereas bulk substrate remains solid phase at room temperature. After PLM the melted layer starts to cool down and recrystallize in the nanosecond time scale which allows the incorporation of Sn into the Ge lattice side with concentration beyond the solid solubility limit [46]. The

influence of PLM process on Sn doped Ge [46] and some other Ge based materials (e.g., As doped Ge) [47] have been studied. According to our investigation $Ge_{1-x}Sn_x$ alloys with up to 1.5% Sn can be obtained by ion implantation and PLM. In the meantime the strain is not released during the bottom-up epitaxy.

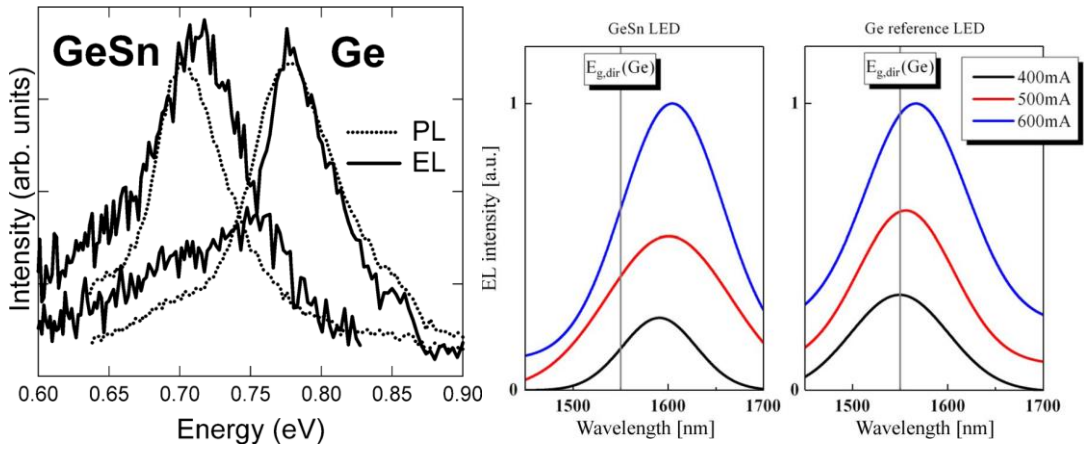

Figure 2.1.5 (left) EL and PL spectra from the Ge / Si and GeSn / Si heterostructural p-i-n diodes compared with room temperature PL spectra from Ge and GeSn layers. From ref. [26]. (right) Comparison of the electroluminescence spectra of GeSn heterostructural vertical LED with Ge LED. From ref. [48]. A clear redshift of luminescence from GeSn in comparison with Ge is observed for the two graphs.

Room temperature electroluminescence has been reported from a GeSn light-emitting diode prepared by MBE or CVD, as shown in Figure 2.1.5. The clear redshift of luminescence from GeSn compared with Ge proves the bandgap modification of GeSn and its promising prospects in optoelectronic applications. Our solution of synthesis of high quality monocrystalline GeSn by ion implantation and PLM, which is efficient and suitable for mass production, can probably be another approach to the fabrication of GeSn-based light emitting devices.

2.2 Dilute nitride $GaAs_{1-x}N_x$ alloys

GaAs is the most commonly used semiconductor material besides group-IV semiconductors of Si and Ge. In virtue of its direct bandgap and outstanding optical and electrical performances, GaAs as well as GaAs based LMAs is widely used in the manufacture of devices such as microwave frequency devices, infrared light-emitting diodes and laser diodes, light detectors, high efficiency solar cells, and optical windows. The growth of bulk and thin film GaAs has been well developed. Therefore, GaAs and GaAs based alloys have also been used as substrates or buffer layers for the growth of various kinds of semiconductor thin films and structures.

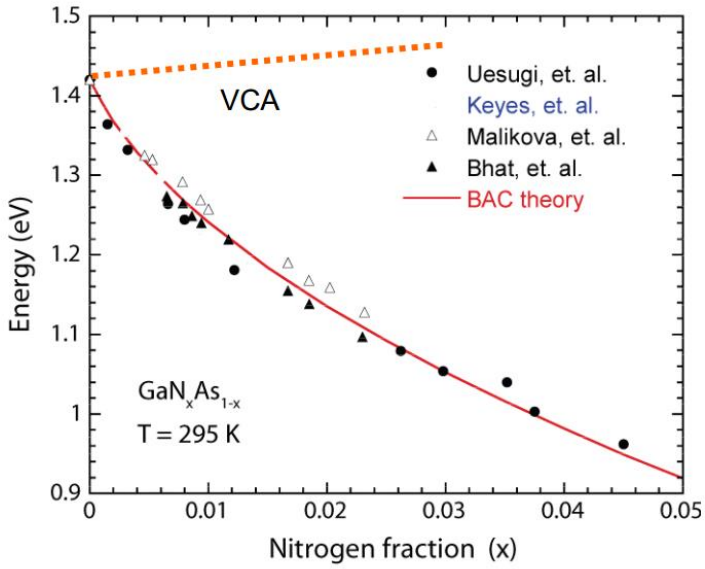

Figure 2.2.1 Bandgap shrinkage of $GaAs_{1-x}N_x$ at room temperature with increasing nitrogen fraction [49]. The red linear dotted line shows the expected result according to virtual crystal approximation (VCA) [2,3]. The red solid curve is the result calculated by BAC theory. The experimental data are adapted from ref. [50-52].

Nitrogen atom is an isoelectronic substituent for arsenic in GaAs. In virtue of its considerably smaller atomic size and stronger electronegativity (i.e.,

highly mismatched), a small amount of nitrogen substituting for arsenic in GaAs (i.e. $GaAs_{1-x}N_x$ dilute nitride) will lead to a pronounced bandgap shrinkage [10,15,53,54], as shown in Figure 2.2.1. At room temperature, the GaAs bandgap decreases by 120~180 meV per atomic percent of nitrogen doping [15,55,56]. This discovery has opened an interesting possibility of using dilute nitride HMAs for long wavelength optoelectronic devices [57,58]. Except for the common applications of light emitters and absorbers, dilute nitride $GaAs_{1-x}N_x$ after proper defect engineering has also been reported as a candidate for spin filter operating at room temperature and zero magnetic field [59], which afford us another possibility of the spintronic applications.

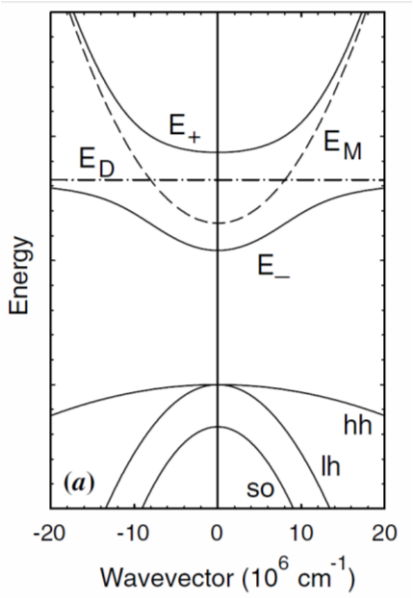

Figure 2.2.2 Schematic view of band anti-crossing (BAC) mode applied to $GaAs_{1-x}N_x$. The N-induced donor level (dash-dotted line, E_D) interacts with the extended states of the conduction band (dashed line, E_M), hence resulting in the restructured E_- and E_+ subbands. From ref. [49]

Band anti-crossing (BAC) model has been developed to analyze the band structure variation induced by N-doping in GaAs and the pressure and composition dependencies on the bandgap [4,9,10]. The theory of BAC applies a simple model of two interacting models: one is the extended states of

the GaAs matrix, the other is the localized N states. The interaction of the two states can be treated as a perturbation which leads to the following eigenvalue problem [10]:

$$\begin{vmatrix} E - E_M & V_{MN} \\ V_{MN} & E - E_N \end{vmatrix} = 0,$$

where E_M and E_N are the energies of the GaAs conduction band and of the N level relative to the maximum of the valence band, respectively; and V_{MN} is the matrix element describing the mixing and anticrossing of the two states. The two solutions of the equation can be written as [10]:

$$E_{\pm} = (E_N + E_M \pm [(E_N - E_M)^2 + 4V_{MN}^2]^{1/2})/2$$

As depicted in Figure 2.2.2, the energy level of the highly electronegative isoelectronic N induced localized state (E_D) is at about 0.25 eV above the conduction band minimum and resonant with the conduction band. The interaction between the localized isoelectronic state and the conduction band state results in a dispersion of the two conduction subbands E_- and E_+. The lower conduction subband (marked as E_-) narrows drastically as the energy position of the N-induced donor level E^d (E_D in Figure 2.2.2) moves down relative to the bottom of the conduction band. Narrowing of the band indicates a gradually increased contribution of the localized nature to the lowest subband, leading to a highly nonparabolic dispersion relationship that induces a broadening of the energy states. [49]

In the meantime, N-incorporation into GaAs will also lead to a broadening of the near band-edge (NBE) luminescence, which has not only been observed experimentally but also been explained in theory. J. Wu *et al.* used the many-impurity Anderson model to evaluate the interaction between the randomly distributed localized states and the extended states in $GaAs_{1-x}N_x$ and calculated the results with the single-site coherent-potential approximation (CPA). The calculations reproduce the BAC model results for the restructuring of the conduction band. This approach also yields information on the electronic level broadening which is used to determine the broadening of the optical

transitions and to calculate the free-electron mobility [3]. As an example, Figure 2.2.3 shows the dispersion relations for $GaAs_{1-x}N_x$ (x=0.005) near the Brillouin-zone center. The phenomenon of the NBE PL broadening induced by N-doping has also been observed in our experiments and will be presented in Chapter 5.

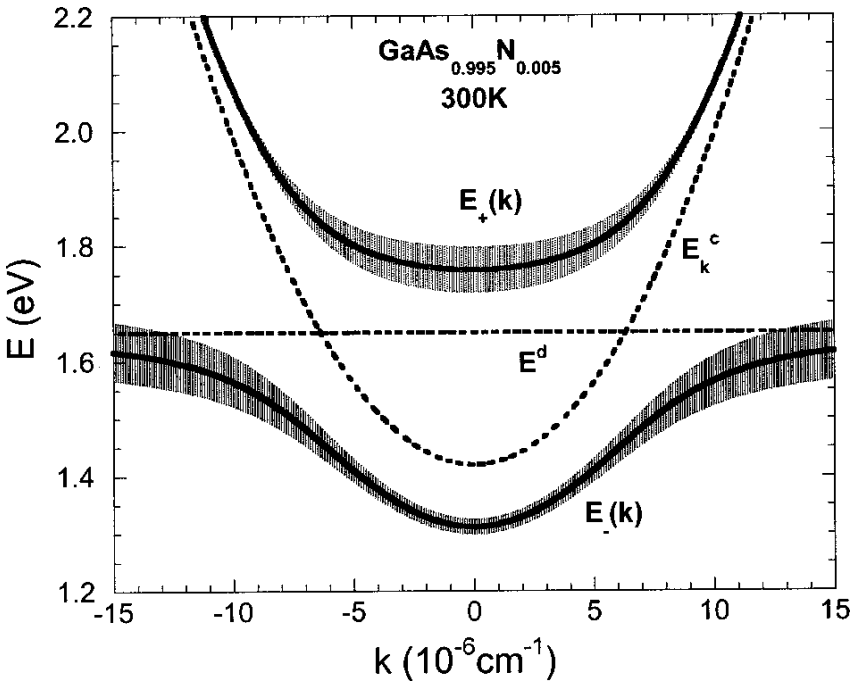

Figure 2.2.3 Schematic view of conduction band restructuring according to BAC model applied to $GaAs_{1-x}N_x$ for x=0.005. The broadening of the dispersion curves (shadows in the figure) of the newly formed subbands illustrates the hybridization induced energy uncertainties. From ref. [3].

Due to the low solubility of N in GaAs, it is a constant challenge to fabricate high quality $GaAs_{1-x}N_x$ under equilibrium conditions. Ion implantation is an efficient method for the doping of N into GaAs beyond its solid solubility. The amorphized of the top layer during implantation can be recrystallized by post-implantation ultra-short annealing. The various types of defects in GaAs and GaAs based materials can lead to a critical downgrade of the materials. Therefore to control the quantity of the defects is one of the main issues for

GaAs based materials modified by ion implantation and annealing, especially for their optoelectronic applications. High density of defects can reduce the conductivity of the materials and prevent the excitons from radiative recombination hence quenching the luminescence.

In Chapter 5, the room temperature near band-edge (NBE) emission in the photoluminescence (PL) spectra observed from implantation-prepared $GaAs_{1-x}N_x$ is presented. The clear NBE luminescence shown from our FLA treated $GaAs_{1-x}N_x$ indicates its good quality and promising potential for light emitting applications. According to the NBE peak shift, the activated N fraction is determined to be x_{act1}=0.19% for x_{imp1}=0.38% and x_{act2}=0.28% for x_{imp2}=0.76% for single flashed samples. The activated N fractions are further increased to x_{act1}(2FLA)=0.30% for x_{imp1}=0.38%, x_{act2}(2FLA)=0.34% for x_{imp2}=0.76%, respectively, by applying double FLA. The concentration of the activated N concentration suggests a remarkably high activation efficiency achieved by ion implantation and FLA.

2.3 Defect engineering in $GaAs_{1-x}N_x$ alloys and other GaAs based materials for optoelectronic applications

As a matter of fact that 1.30 μm and 1.55 μm is the second and the third transmission window of optical fibers, many approaches have been designed on GaAs related matrices to achieve emissions at these two wavelengths. One approach is to shrink the bandgap by lightly mismatched alloying with narrower bandgap materials such as InAs or InP, *i.e.* to form ternary / quaternary alloys such as InGaAs/InGaAsP. Another approach focuses on incorporating different quantum dots into the GaAs matrices, e.g., self-assembled InAs quantum dots (QD) [60]. Depending on the size of the quantum dots, the peak position of the luminescence can be easily tuned to fit the transmission windows of optical fibers. Besides the two common approaches, proper defect

engineering can also be used to achieve luminescence which fits the windows for optical communication. The defect related luminescent bands in GaAs are in the spectral range between 0.8 eV and 1.35 eV (1550 nm – 910 nm), consisting of gallium and / or arsenic vacancies / interstitial complexes [61,62]. The luminescence from some of the defect levels can be relatively immune to temperature changes. For practical applications, the stability at a broad temperature range is one of the key issues to evaluate the performance of the devices.

In Chapter 6, the defect related luminescence at 1.30 μm from $GaAs_{1-x}N_x$ prepared by implantation and FLA will be presented. This luminescence is quasi-stable in the respects of wavelength and intensity with operating temperature ranging from 20 K to room temperature. The influence of implantation and / or different dopants (isoelectronic dopants: N, P, and In; p-type dopants: Zn and Mn) in GaAs on the 1.30 μm luminescence has been investigated. With indium-doping, the 1.30 μm luminescence has been greatly enhanced by more than two orders of magnitude compared with the virgin GaAs after FLA treatment. Based on the results, the regime of this luminescence has been deduced.

Chapter 3 Experimental Techniques

3.1 Ion implantation, interaction between ions and solids

Ion implantation has been applied to the standard production line of integrated circuits as a mature doping technique for semiconductor materials. Compared with other doping techniques, ion implantation has a number of advantages, including but not limited to the points listed below [63]:

- High efficiency, good homogeneity and reproducibility.
- Non-equilibrium doping process, possibility of beyond-solubility-doping.
- Accurate control of the doping concentration by manipulating the implantation fluence.
- Isotopic selection of ion beams based on mass separation.
- Simple masking methods to make lateral patterns for devices.

As discussed in the first two chapters, highly mismatched alloying is in most cases beyond the solid solubility of the host matrices. In this case, ion implantation is likely to be an applicable method to achieve highly mismatched doping in semiconductors discussed in this thesis.

An implanted ion with certain kinetic energy in solids will undergo a number of collisions with the host atoms, during which the kinetic energy will be transferred to the host atoms. The energy transfer between ion and host atoms can be through elastic collision (i.e. no net conversion of kinetic energy into other forms through collision) or inelastic collision (i.e. there is conversion of kinetic energy into other forms such as lattice vibration). As one of the consequences of the elastic collision, the impacted host atom can be displaced from the lattice site due to the high kinetic energy gained through the collision. In addition, it is possible that these displaced atoms still have enough energy to displace others, resulting in a cascade of recoiled atoms [63]. In the case of inelastic collision, the kinetic energy can be transferred to the electrons of the

host atoms, exciting the host atom to higher energy level. Then the exciting energy can be transferred to the lattice through non-radiation transition of the excited electrons or to the photons generated through radiation transition. The former case will bring about an enhanced lattice vibration, i.e. a rising temperature of the host material.

Due to the energy transfer, the implanted ions will lose their kinetic energy and finally be trapped in the host matrices. The stopping effect, which can be evaluated as the energy loss per unit penetration depth dE/dx, is roughly constant in the normal energy range (from several hundred eV to several MeV) of implantation. The projected range R_p is proportional to the initial incident ion energy. In the case of an amorphous target material, the depth profile of the implanted ions follows Gaussian stopping distribution, which is related to the projected range R_p, the standard deviation ΔR_p, and the implantation fluence Φ [63]:

$$N(x) = \frac{\Phi}{\sqrt{2\pi}\Delta R_p} exp[-\frac{(x-R_p)^2}{2(\Delta R_p)^2}],$$

where $N(x)$ represents the concentration of the implanted ions at the depth of x. Accordingly, the peak concentration N_p can be calculated as:

$$N_p = \frac{\Phi}{\sqrt{2\pi}\Delta R_p},$$

which locates at R_p.

Dopant ions implanted with a certain kinetic energy will finally be distributed as a Gaussian-shaped depth profile. With a multiple implantation (i.e., ions are implanted with a combination of two or more energies for different fluences to compensate the Gaussian distribution), it is possible to overcome the inhomogeneity of the Gaussian distribution and form a box-like depth profile, as shown in Figure 3.1.

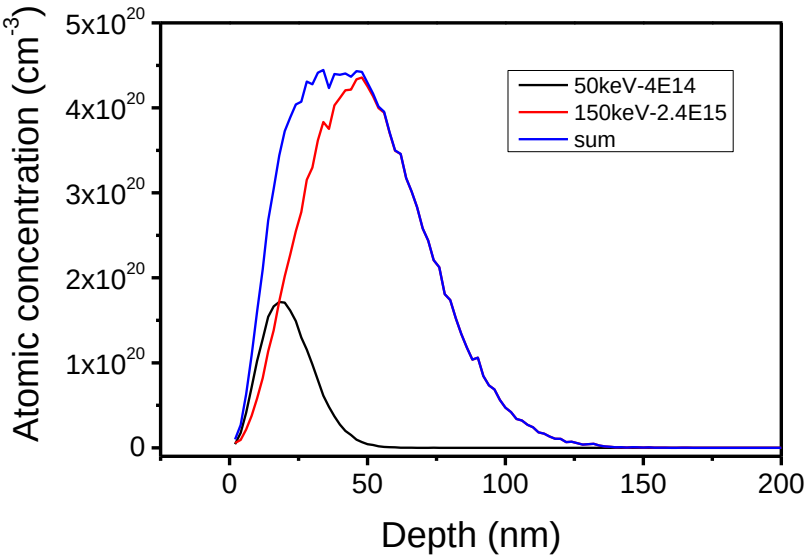

Figure 3.1 Depth profile of Sn implanted with 50 keV for a fluence of 4×10^{14} cm^{-2} and 150 keV for a fluence of 2.4×10^{15} cm^{-2} in Ge wafer. The result was simulated by SRIM code [19].

The implantation energy depends on the composition of host and the implanted atoms, the atomic density of the host material, and the required implantation depth. In our case of the synthesis of HMAs of dilute nitride III-V_{1-x}-N_x and $Ge_{1-x}Sn_x$, the kinetic energies of the implanted ions are set to from tens of keV to hundreds of keV in order to form a homogeneously doped layer of up to about 200 nm in depth. In this energy range, elastic collision dominates during the implantation process, hence forming a large number of defects. The detailed experimental parameters will be introduced in the following chapters for each material.

Considering the elastic collision during implantation discussed above, the uniformity of the lattice will be downgraded due to the recoiling process of host atoms from the lattice. Depending on the mass, the kinetic energy, and the fluence of the dopant ions, the as-implanted region can be partially or even completely amorphized. To reform or restore the lattice from the amorphized structure and to activate the dopants, post-implantation annealing is required.

Annealing is a heating process which is widely applied in semiconductor device fabrication in order to modify the properties of the materials. It is a standard process after ion implantation to activate the dopants and to repair the damage caused by implantation. The two most commonly used annealing techniques are furnace annealing (FA) and rapid thermal annealing (RTA). FA process can last between minutes to hours, whereas RTA works on a time scale of several seconds. The time range for both FA and RTA allows samples to reach nearly thermal equilibrium condition under which the self-organization is in progress to modify the material. However, under thermal equilibrium condition, the dopant beyond solubility tends to segregate from the host material to form clusters / grains or even evaporate for some elements with low gasification temperature, which makes FA and RTA not suitable for the case of highly mismatched alloying. Therefore, ultra-short annealing, during which the materials cannot reach thermal equilibrium condition, can be applied as a solution for the synthesis of HMAs. The two ultra-short annealing techniques applied in this thesis are pulsed laser melting and flash lamp annealing, both of which use ultra-short light pulse to achieve ultra-fast heating and consequent ultra-fast cooling.

3.2 Pulsed laser melting (PLM)

Pulsed laser melting is an ultra-fast heating process on the surface of the materials with a single laser pulse or repeating laser pulses, which is used to manipulate the microstructure of the thin film through a melting-resolidification process. In our case a Coherent XeCl excimer laser with 308 nm wavelength and 28 ns pulse duration was applied. The laser spot was uniformized and focused by a fly-eye homogenizer as a 5×5 mm^2 square spot. The energy of the spot was manipulated by a manual attenuator.

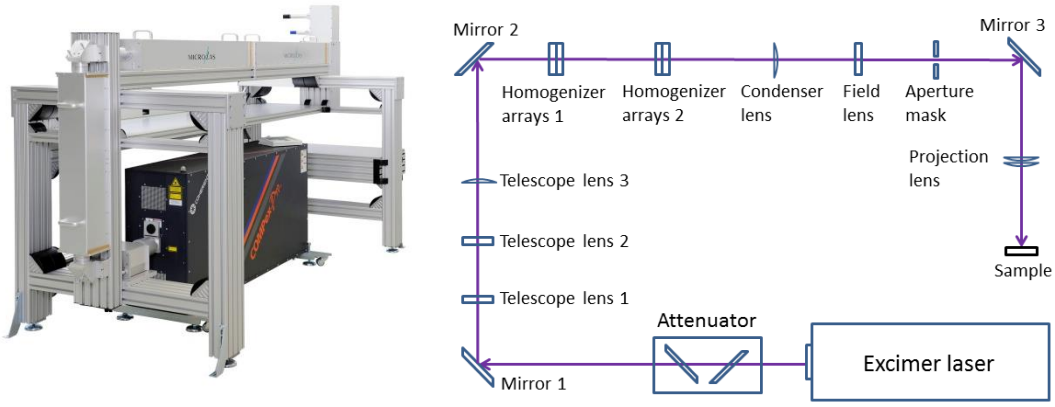

Figure 3.2.1 (left) Excimer laser system applied for PLM. (right) Schematic view of the homogenizing and focusing light path in the PLM system.

During the PLM process, electrons in the materials can absorb photons, and be excited to higher energy levels. Thus, the energy of the photons will be converted to the potential energy of the excited electrons. In the case of PLM to a semiconductor, electrons in the valence band of the semiconductor can absorb photons with higher energy than its bandgap and be excited to higher energy levels in the conduction band, leaving holes in the valence band. The electrons in the conduction band can also be excited to higher energy levels. Consequently, the excited electrons will quickly relax from these high energy levels to a meta-stable level (i.e., conduction band minima) via small step transitions. Normally, this process is in the absence of generation of photons, i.e., a non-radiative transition. Then, the final transitions of the excited electrons occur through the bandgap, so that the excited electrons relax back to the ground state and recombine with holes. This transition can be either radiative or non-radiative. The non-radiative transition occurs more often for a semiconductor with an indirect bandgap than that with a direct bandgap.

The lost potential energy of the electrons through non-radiative transitions will be transferred to the nuclei, thereby enhancing the vibration of the lattices. From the macro point of the view, the energy of the light will convert to heat through the excitation and following non-radiative transitions of electrons. The

surface layer can be melted due to the obtained thermal energy after light irradiation with high energy density. According to the absorption coefficient of Ge for 308 nm light [64], more than 90% of the photons are absorbed within the first 20 nm in our case of PLM on Ge. Because of the thermal conduction from the surface to the deeper region, the liquid-solid interface will move to deeper with a relatively high speed (a few m/s) [46,65]. Therefore, the melted layer is usually deeper than the range of light absorption.

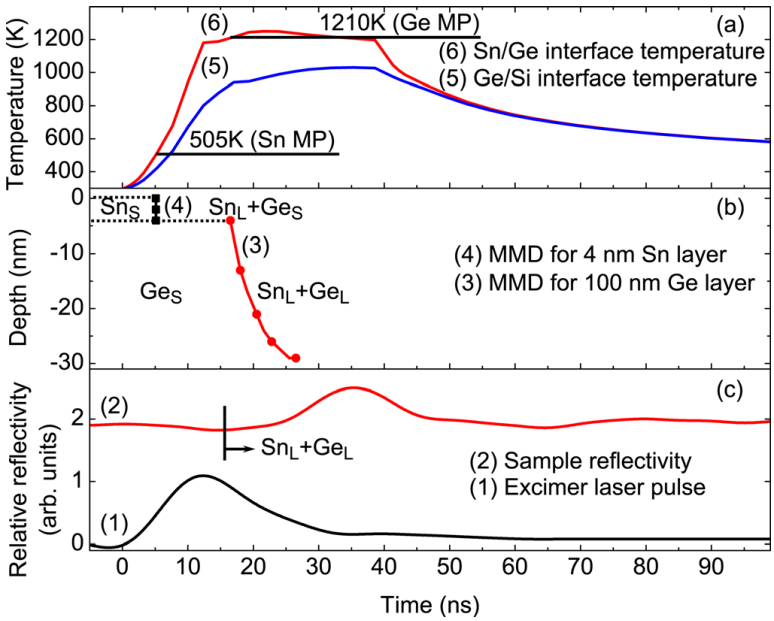

Figure 3.2.2 Temporal evolution of the (a) calculated interface temperatures, (b) calculated depth of solid-liquid transition, and (c) in-situ measured reflectivity, caused by a laser pulse of 0.2 J/cm^2. From ref. [41].

Figure 3.2.2 shows the temporal evolution of a pulsed ArF laser (wavelength 193 nm, pulse duration 25 ns) melting process on a MBE grown structure of Sn (4 nm) / Ge (100 nm) on Si substrate. The reflectivity change during the phase transition (Figure 3.2 (c)) mainly originates from the melting and solidification of the Ge layer [41], which indicates a similar melting time to the laser pulse duration.

Considering that the thermal budget on a unit area of a Ge wafer is low from a nanosecond pulsed laser (between 0.2 J/cm^2 and 0.7 J/cm^2), the melting region should be limited within the depth of about 2 μm. If we take the melting induced reflectivity increase and the temperature rise of the melted region in this non-equilibrium process into consideration, the calculated melted depth will be even smaller. Since the photons are absorbed as an exponential depth profile with a large absorption coefficient, the temperature gradient of the melted layer and the solid substrate should exhibits a steep decreasing trend [46]. Therefore, the most part of the substrate remains at ambient temperature. This causes a bottom-up resolidification process beginning at the liquid-solid interface. In the case of Ge, the solidification front (i.e., the solid / liquid interface) moves at a velocity of a few m/s, and the quenching rate can reach up to 10^9 K/s. Because the sharp gradient of temperature depth profile due to the strong surface absorption and ultrashort irradiation duration promotes the high velocity of the solidification front, diffusion of species is prevented / limited. Therefore, the dopants become trapped under the growing solid interface in a process known as solute trapping [46]. “It has been demonstrated extensively that solute trapping represents a departure from even local thermodynamic equilibrium at the interface, resulting in incorporation of concentrations 10^2 to 10^3 times the maximum solubility from phase diagrams” [66]. If the melted layer is designed deeper than the amorphized layer by ion implantation, the melted layer can epitaxially recrystallize during the resolidification process, with the crystalline substrate underneath acting as a template for the epitaxial recrystallization [46].

3.3 Flash lamp annealing (FLA)

The nanosecond range PLM can achieve high enough temperature to melt the sample surface and activate the implanted dopant [46]. However, a large quantity of defects can be produced during the liquid phase epitaxy regrowth, especially for the cases of III-V semiconductors due to their natural complexity. The millisecond range FLA induced solid phase regrowth can be considered as a compromise between the ultra-short PLM and standard RTA or FA.

In the case of flash lamp annealing, the ultra-short light pulse used to heat up the materials is provided by flash lamps. The energy conversion from light to heat during FLA is similar to that for PLM described above. FLA allows a fast heating up of solid surfaces with a single light flash whose pulse duration ranges from several hundred microseconds to several milliseconds. FLA allows the specific thermal modification of surface layers with or without a reduced thermal exposure of the whole solid body by applying different flash duration. Similar to PLM, thermal equilibrium cannot be reached during the millisecond range heating and cooling process for normal semiconductors, according to their thermal conductivities. Therefore, it can also be applied as a solution to the above-solubility doping.

Figure 3.3.1 shows a schematic view of a typical FLA chamber. The upper part above the sample processing chamber is the main FLA module. An array of parallelly connected Xe-lamps with a reflector behind is installed to provide a homogeneous flash to a large area, which makes FLA suitable for mass production. In order to achieve high temperature or to control the strain introduced by inhomogeneous heating of the surface and the deeper region of the sample, a pre-heating module consisting of an array of continuous halogen lamps is installed under the sample processing chamber. Two pieces of quartz plate, which are transparent for near-UV and visible light, are applied to form a

sample processing chamber in order to separate the air and the protection ambience filled inside.

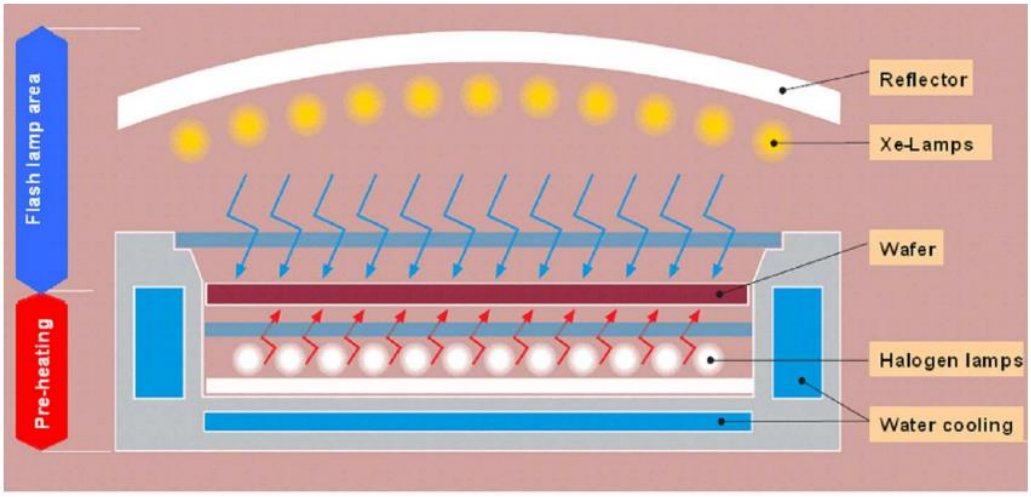

Figure 3.3.1 Schematic view of the FLA system. Adapted from ref. [21]

The pulsed energy is provided by high voltage charged capacitors. Therefore the flash duration can be tuned by modifying the discharge R-C circuit. During the discharge process, the voltage applied to the parallelly connected flash lamps exhibits an exponential decay:

$$V(t) = V_0 \cdot e^{-t/RC},$$

where V_0 is the voltage of the capacitor at time t = 0, R and C are the resistance and the capacity of the discharge circuit, respectively. According to this formula, it is possible to prolong the discharge time by increasing the resistance and /or the capacity in the circuit. The pulse duration applied in this thesis is 3 ms and 20 ms.

In principle, any sample that is able to absorb the light in the spectrum of Xe-lamp can be annealed by this FLA system. The highest annealing energy fluences for 3 ms and 20 ms flash duration are about 100 J/cm^2 and 250 J/cm^2, respectively. The achievable final temperature of the annealed surface layer could be more than 2000 °C depending on the intensity of the light flash and on the optical properties of the flash lamp annealed material. In principle, the

melting point can be reached for most of the semiconductor materials. However, the mobility of the species is much higher in liquid phase than that of solid phase. In this case, critical segregation of the dopant above solubility can take place in millisecond time range. In addition, for GaAs based materials, massive defects can be generated from the liquid phase recrystallization. For this reason, the annealing temperature of the sample surface was practically controlled below its melting point.

Due to the large absorption coefficient of visible light for the narrow bandgap semiconductors (GaAs and Ge in this thesis) [64], the absorption of the irradiation mainly take place in the surface layer within the depth of tens or hundreds of nanometers. The temperature rise in the deeper region is a consequence of the heat conduction from the surface, which will be smaller than the surface layer and exhibit as a decay trend with increasing depth.

A calculation of the temperature evolution in Si wafer for different depths during 3 ms and 20 ms FLA is shown in Figure 3.3.2. According to the calculation, the actual annealing time at high temperature is comparable with the light pulse duration of FLA. In addition, the depth profile of the peak temperature is different for FLA with different annealing time. With the same annealing temperature on surface, the temperature rise is higher for a longer FLA pulse duration at the same depth, as shown in Figure 3.3.2. In the case of heating the surface of a silicon wafer from 650 °C up to 1300 °C by 20 ms FLA, the temperature at the depth of 800 μm rises for about 300 °C. On the other hand, for the same temperature rise on surface by 3 ms FLA, the temperature at the depth of 800 μm rises for only about 50 °C. Therefore, FLA can be considered as a low temperature processing technique, which can avoid the thermally induced negative effects to the substrate, *e.g.*, oxidation, decomposition, and defect generation.

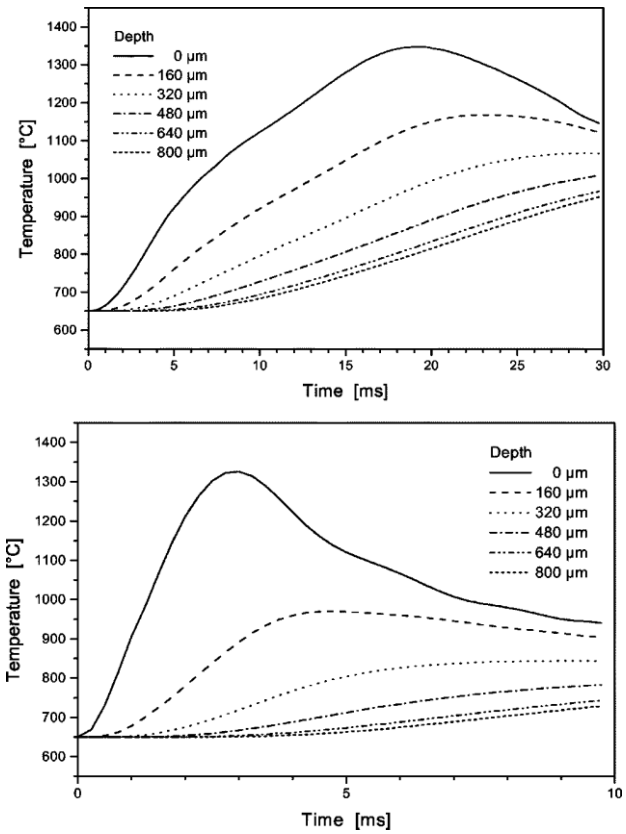

Figure 3.3.2 Temperature evolution on time for different depth of an 800 µm thick silicon wafer during FLA to 1300 °C on surface at a preheating temperature of 650°C for a pulse duration of 20 ms (upper part) and 3 ms (lower part) From ref. [20].

Considering the fact that the thermal conductivity of GaAs (55 $W \cdot m^{-1} \cdot K^{-1}$) and Ge (60 $W \cdot m^{-1} \cdot K^{-1}$) is less than that of Si (149 $W \cdot m^{-1} \cdot K^{-1}$), the depth profile of the rising temperature in Ge and GaAs should be narrower and sharper than that in Si wafer. Therefore the influence of heating on the substrate should be less than that on Si.

In the following chapters, the influence of PLM and FLA on semiconductors (i.e., recrystallization of amorphous layers, incorporation of implanted dopants, and manipulation of defects, etc.) will be presented and discussed.

Chapter 4 $Ge_{1-x}Sn_x$

$Ge_{1-x}Sn_x$ alloys synthesized by ion implantation and pulsed laser melting

4.1 Introduction

Group IV semiconductor alloys have drawn substantial attention for their potential applications to optoelectronic devices which are capable of integration with the existing silicon-based integrated circuit (IC). Germanium exhibits a pseudo-direct gap behavior because the energy difference between its direct (Γ band minimum to valence band maximum) and indirect (L band minimum to valence band maximum) bandgaps is only 136 meV [24,28]. With Sn doping, the energy difference can be further reduced [33]. Monocrystalline $Ge_{1-x}Sn_x$ alloys have been predicted to convert from indirect to direct bandgap semiconductor with proper Sn composition of above 6 *at.* % [26], as a consequence of the faster lowering of the Γ band than the L band with increasing Sn content [24,32,33,41]. Moreover, the $Ge_{1-x}Sn_x$ alloys are also attractive for electronic and optical applications in virtue of their high carrier mobility. Based on these features, the $Ge_{1-x}Sn_x$ system shows a promising perspective of the realization of direct-gap semiconductor optoelectronic devices fully integrated with Si technology [40].

However, it is challenging to achieve $Ge_{1-x}Sn_x$ alloys due to the very low solid solubility (<1 *at.* %) of Sn in Ge [32,67]. Different methods (e.g., molecular beam epitaxy (MBE) [18,31,43], chemical vapor deposition [3,44,68], and magnetron sputtering [39]) have been applied to synthesize $Ge_{1-x}Sn_x$ alloys. S. Stefanov *et al.* have synthesized $Ge_{1-x}Sn_x$ by applying pulsed laser melting (PLM) to an MBE grown structure of thin Sn layer on a virtual Ge layer [41]. Kurosawa *et al.* have applied focused PLM on an MBE grown amorphous

$Ge_{1-x}Sn_x$ layer on SiO_2 in water and obtained crystalline $Ge_{1-x}Sn_x$ with 2 *at.* % of Sn [69]. The influence of PLM process on Sn doped Ge [32,45,46] and some other Ge based materials (e.g., As doped Ge) [47] have been studied. However, high quality monocrystalline $Ge_{1-x}Sn_x$ alloys achieved by Sn-implantation is still a missing part of the story. Ion implantation is an efficient non-equilibrium doping method and is a standard processing technique in IC industry. An approach combining ion implantation and PLM would open a chip technology compatible route to synthesis $Ge_{1-x}Sn_x$. This approach has been employed to synthesize various alloys, e.g., GaAsN [70], GaMnAs [71], and ZnTeO [72], which are challenging by thermal equilibrium methods.

In this contribution, we present the low-temperature synthesis of $Ge_{1-x}Sn_x$ alloys on Ge substrates by ion implantation and PLM during which the temperature rise of the substrate was controlled below 100 °C. Monocrystalline $Ge_{1-x}Sn_x$ alloys with up to 1.5 *at.* % Sn composition have been obtained. The shrinkage of the Ge bandgap induced by Sn-doping was confirmed according to the redshift of the E_1 and $E_1+\Delta_1$ transition from spectroscopic ellipsometry (SE). As a consequence of the above, this technique is promising for the synthesis of high quality $Ge_{1-x}Sn_x$ alloys embedded in the IC process flow for optoelectric devices.

4.2 Experimental Setup

Commercial n-type Ge wafers were implanted with Sn ions of four different fluences (1.4×10^{15} cm^{-2}, 2.8×10^{15} cm^{-2}, 4.2×10^{15} cm^{-2}, and 8.4×10^{15} cm^{-2}) at room temperature. A combination of two implantation energies of 150 keV and 50 keV with a fluence ratio of 6:1 was applied in order to distribute the implanted Sn more homogeneously in the near surface region within the depth of 80 nm. After implantation, the wafers were treated by PLM. A Coherent XeCl

excimer laser with 308 nm wavelength and 28 ns duration was uniformized and focused by a fly-eye homogenizer as a 5×5 mm^2 square spot. Samples were irradiated by one laser pulse at the focus with various energy fluences ranging from 0.2 J/cm^2 to 0.7 J/cm^2. During this high intensity laser process, the near-surface layer including the whole implanted region was melted whereas the bulk substrate remained at ambient temperature. After PLM, the melted layer starts to cool down and recrystallize in nanosecond time range, which allows for the Sn doping beyond the solid solubility limit [46]. The cooling down and recrystallization started from the interface between the melted and solid regions, which resulted in the bottom-up liquid phase epitaxial growth of the $Ge_{1-x}Sn_x$ layer [41].

The structural properties of the $Ge_{1-x}Sn_x$ alloys were investigated by Rutherford backscattering spectroscopy (RBS), micro Raman spectroscopy, X-ray diffraction (XRD), and cross-sectional transmission electron microscopy (TEM). In RBS analysis, the scattered ions were collected with a collimated 1.7 MeV He^+ beam with a 10-20 nA beam current at a backscattering angle of 170°. The channeling spectra were recorded by aligning the sample to make the impinging He^+ beam parallel with the Ge <001> axis. The Raman spectra were collected in a backscattering geometry with a 532 nm Nd:YAG laser excitation, and detected by a liquid-N_2-cooled charge-coupled device. XRD experiments were performed at Rossendorf Beamline (ROBL), European Synchrotron Radiation Facility (ESRF), using an X-ray with wavelength of 1.0781 Å, and the diffracted signal was collected by a one-dimensional Mythen detector. The TEM micrographs were taken using an image-corrected FEI Titan 80-300 microscope operated at an accelerating voltage of 300 keV. The near-ultraviolet-visible SE spectra were measured by a VASE HS-190 ellipsometer.

Determined by RBS, the remaining Sn concentrations of the samples after implantation and PLM are 0.5 *at.* % (atomic percent), 1.0 *at.* %, 1.3 *at.* %, and

1.5 *at.* %, respectively. Because of the low melting point of Sn (~232 °C) and low phase transition temperature of α-Sn and β-Sn (13.5 °C) [100-Bhatia], the melting temperature of $Ge_{1-x}Sn_x$ depends sensitively on the increasing Sn content. Based on the structural properties (i.e., the minimal RBS channeling yield, the strongest Raman crystalline Ge-Ge mode, and the most obvious Sn-induced symmetrical (004) diffraction peak shift), the optimized PLM condition for each Sn concentration (0.60 J/cm^2 for 0.5 *at.* % Sn, 0.50 J/cm^2 for 1.0 *at.* % Sn, 0.40 J/cm^2 for 1.3 *at.* % Sn, 0.34 J/cm^2 for 1.5 *at.* % Sn) was individually selected. The results presented in this chapter are all measured from samples treated with optimized PLM condition.

4.3 Results and discussion

Simulation described in ref. [19] was applied to analyze the composition of the samples from the RBS spectra. The random spectrum of the as-implanted $Ge_{1-x}Sn_x$ reveals a Sn doped Ge layer with a thickness of about 80 nm, together with a short tailing on both shallower side and deeper side (not shown). No channeling effect can be observed from the as-implanted region for both Ge and Sn because of the amorphization caused by implantation. The Sn signal reveals a tendency of diffusion to the near surface region after PLM, forming a Sn-enriched surface layer of about 50 nm and a tailing from the descendent diffused Sn components to the deeper side of around 80 nm. According to the simulation, the Sn concentration after PLM is about 0.5 at. %, 1.0 at. %, 1.3 at. %, and 1.5 at. % in the near-surface region for the four samples presented in this chapter.

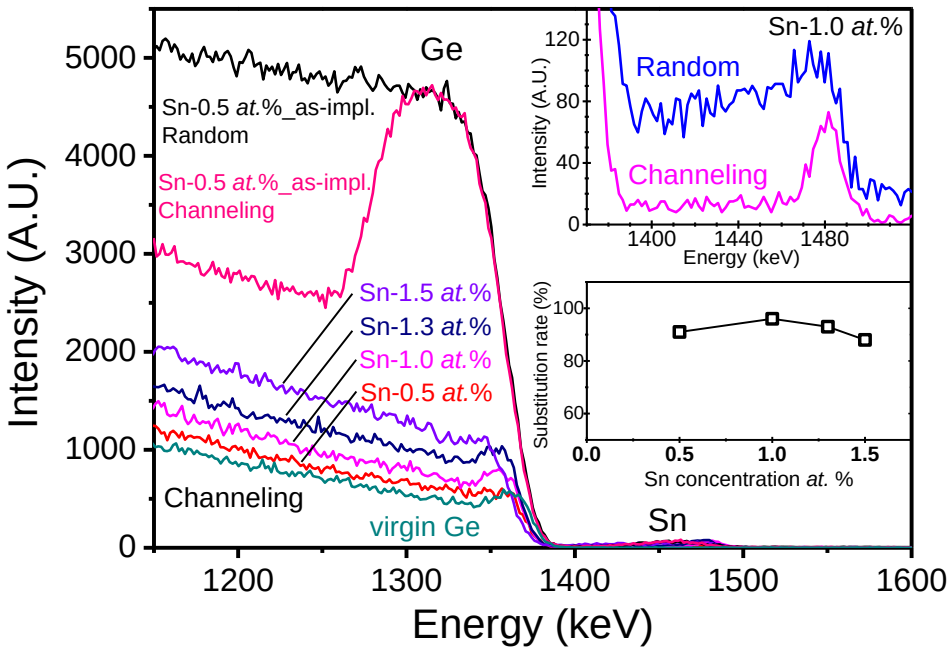

Figure 4.1 <001> channeling RBS spectra from PLM treated $Ge_{1-x}Sn_x$ samples with Sn concentration ranging from 0.5 *at.* % up to 1.5 *at.* %. Random and channeling spectra from 0.5 *at.* % Sn as-implanted sample (marked as Sn-0.5 *at.* %_as-impl.) as well as channeling spectrum from virgin Ge wafer are also shown for comparison. The upper inset provides a magnification of random and channeling Sn signals from PLM treated $Ge_{1-x}Sn_x$ with 1.0 *at.* % Sn. The lower inset shows the substitutional fraction of implanted Sn for different Sn concentrations.

For the 1.0 at. % Sn implanted sample, the channeling spectrum exhibits a minimum yield ratio to random spectrum of about 13% for Ge and 16% for Sn in the Sn-doped region. The substitutional fraction for Sn (i.e., the ratio of substitutional Sn at the Ge lattice sites to total implanted Sn) can be calculated as (1-16%)/(1-13%)=96% [73]. The substitutional fractions of the other samples with 0.5 at. %, 1.3 at. %, and 1.5 at. % Sn are calculated as 91%, 93%, and 88%, respectively. The channeling effects of both Ge and Sn from the PLM-treated samples confirm a complete recrystallization of the implanted layer and the incorporation of Sn into the lattice sites of Ge. The increase of

the channeling yield value from samples with higher Sn concentration suggests a slightly increased amount of disorder induced by a higher doping level of Sn for its highly mismatched atomic size and lattice constant with the host Ge.

The Raman spectra from the as-implanted and PLM-treated $Ge_{1-x}Sn_x$ samples are shown in Figure 4.2. Note that the penetration depth of a 532 nm laser used for the Raman investigation in Ge is about 40 nm [64]. Therefore, any influence of the Ge wafer beneath the prepared $Ge_{1-x}Sn_x$ alloys on the recorded Raman spectra can be excluded. The Ge-Ge Raman mode from the virgin Ge wafer is located at 300.6 cm^{-1} (see inset). After implantation, the Ge-Ge peak shifts towards 269 cm^{-1} together with remarkable broadening, indicating an amorphized implanted layer. PLM process on the implanted layer leads to the reformation of the crystalline structure, which is confirmed by the appearance of the Ge-Ge phonon mode at around 300 cm^{-1}. The variations of the peak position and the FWHM with Sn concentration from 0 to 1.5 *at.* % are shown in the inset. The peak shift of the Ge-Ge related phonon mode in $Ge_{1-x}Sn_x$ alloy can be attributed to lattice expansion and disorder caused by Sn incorporation [32,39,74]. The value of the shift of the Ge-Ge Raman mode is smaller than that reported for the strain released $Ge_{1-x}Sn_x$ alloys in ref. [74]. This is due to the existence of compressive strain in our samples, which is confirmed by the following XRD reciprocal space mapping (RSM). Correspondingly, the phonon mode becomes broader with increasing Sn content. For the samples with more than 1.0 *at.* % of Sn, the peak position and the band width of the phonon mode vary more obviously, which can be attributed to the consequences of the above-solubility doping of the highly mismatched Sn, which is consisted with the RBS channeling data presented above.

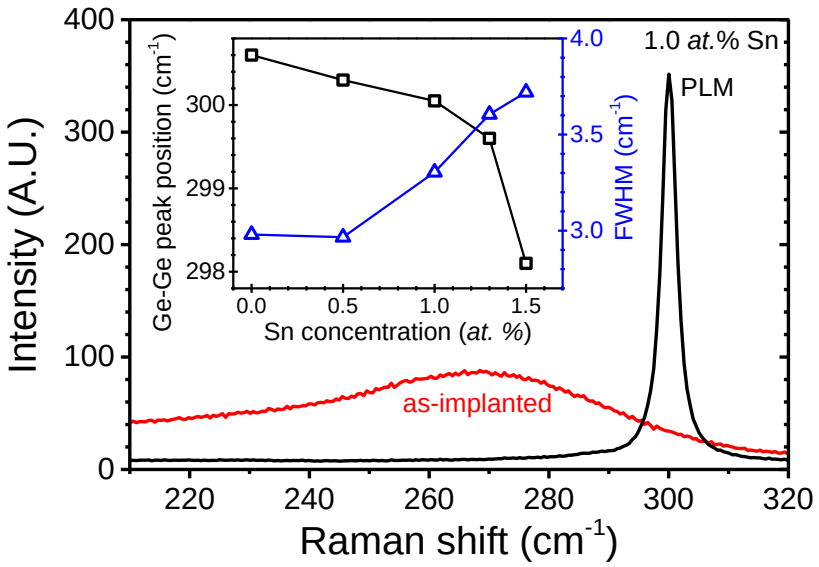

Figure 4.2 Micro-Raman spectra of the as-implanted and PLM-treated $Ge_{1-x}Sn_x$ with 1.0 *at.* % of Sn, marked as as-implanted and PLM, respectively. The inset shows the peak shift (Ge-Ge peak position) and broadening (full width at half maximum, FWHM) of the Ge-Ge phonon mode from the $Ge_{1-x}Sn_x$ alloys with different Sn concentration after PLM.

The influence of Sn doping with different concentration on the $Ge_{1-x}Sn_x$ (004) XRD peak is shown in Figure 4.3 (a). The Ge (004) peak from the as-implanted sample has similar line shape but the integrated intensity is more than one order of magnitude weaker compared to the virgin Ge wafer and the PLM-treated samples. Due to the complete amorphization of the Sn-implanted near surface layer, only the crystalline structure of the Ge substrate below the Sn-implanted region is able to contribute to the (004) diffraction peak. The comparable Ge (004) peak intensities for the virgin and the PLM-treated $Ge_{1-x}Sn_x$ samples indicate the good recrystallization of the as-implanted region after PLM. Moreover, an additional peak appears at the left side of the Ge (004) reflection for the PLM-treated samples. According to Bragg's Law, the appearance of such a peak suggests a layer with a larger lattice parameter than Ge. The Sn-incorporation expands the reformed lattice, which causes the

shift of the $Ge_{1-x}Sn_x$ (004) peak to a lower angle. With increasing Sn-concentration this effect is more pronounced.

The influence of Sn doping with different concentration on the $Ge_{1-x}Sn_x$ (004) XRD peak is shown in Figure 4.3 (a). The Ge (004) peak from the as-implanted sample has similar line shape but the integrated intensity is more than one order of magnitude weaker compared to the virgin Ge wafer and the PLM-treated samples. Due to the complete amorphization of the Sn-implanted near surface layer, only the crystalline structure of the Ge substrate below the Sn-implanted region is able to contribute to the (004) diffraction peak. The comparable Ge (004) peak intensities for the virgin and the PLM-treated $Ge_{1-x}Sn_x$ samples indicate the good recrystallization of the as-implanted region after PLM. Moreover, an additional peak appears at the left side of the Ge (004) reflection for the PLM-treated samples. According to Bragg's Law, the appearance of such a peak suggests a layer with a larger lattice parameter than Ge. The Sn-incorporation expands the reformed lattice, which causes the shift of the $Ge_{1-x}Sn_x$ (004) peak to a lower angle. With increasing Sn-concentration this effect is more pronounced.

To determine the strain of the sample, XRD RSM was conducted around the (620) diffraction. Figure 4.3 (b) shows the RSM for the (620) reflection from the $Ge_{1-x}Sn_x$ alloy with Sn concentration of 1.0 *at.* %. Any pair of coordinates (q_x, q_z) in the map corresponds to the incident and the exit angles of the distorted cubic crystal following the equations given below:

$$q_x = K[\cos(2\theta)-\cos(2\theta-\omega)],$$

$$q_z = K[\sin(2\theta)+\sin(2\theta-\omega)],$$

where $K=2\pi/\lambda$, λ is the wavelength of the X-ray, 2θ is the exit angle, $2\theta-\omega$ is the incident angle.

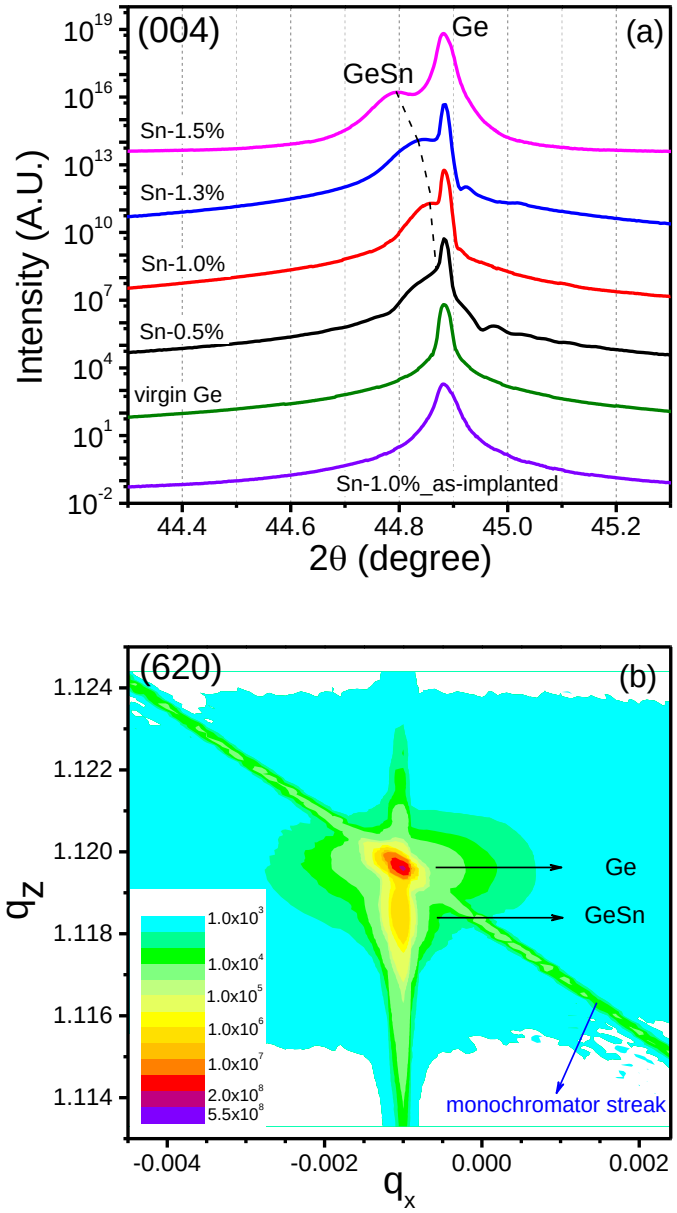

Figure 4.3 (a) Symmetric XRD θ-2θ scans around Ge (004) diffraction maximum of $Ge_{1-x}Sn_x$ alloy with Sn concentration ranging from 0.5 *at.* % up to 1.5 *at.* % after optimized PLM treatment. The diffraction patterns from virgin Ge wafer and 1.0 *at.* % Sn as-implanted sample are shown for comparison. The axis of diffraction intensity is in logarithmic scale. The presented curves from $Ge_{1-x}Sn_x$ alloys after PLM have been vertically offset by three orders of magnitude for clarity. The dashed line shows the peak shift of $Ge_{1-x}Sn_x$. (b) Reciprocal space map of (620) diffraction peak from $Ge_{1-x}Sn_x$ with 1.0 *at.* % of Sn content.

Similar to the (004) reflection discussed above, a characteristic $Ge_{1-x}Sn_x$ peak is visible at a comparable position in the (620) reflection. This $Ge_{1-x}Sn_x$ peak is allocated at the same q_x position as the Ge substrate peak, which suggests that the $Ge_{1-x}Sn_x$ alloy is fully strained on the Ge substrate. The existence of the strain between the $Ge_{1-x}Sn_x$ layer and the Ge substrate suggest that PLM induced liquid phase epitaxy is a strain preserving method, which provides the possibility to enhance the carrier mobility [75,76]. Moreover, a tensile strain in $Ge_{1-x}Sn_x$ by doping Si into $Ge_{1-x}Sn_x$ layer [44] or by introducing a proper buffer layer (e.g., InGaAs [74]) can probably be kept after ion implantation and PLM. Considering the fact that the tensile strain can be applied to reduce the energy difference between Γ band and L band, it is possible to apply the tensile strain to reduce the minimum Sn concentration needed for realizing direct bandgap $Ge_{1-x}Sn_x$ alloys [24,28].

Cross-sectional TEM analysis was conducted to examine the crystalline structure of the $Ge_{1-x}Sn_x$ alloys with 1 *at.* % Sn after PLM. Oriented in <110> zone axis, the single-crystalline Ge wafer appears dark in the bright-field TEM image as presented in Figure 4.4. The contrast does not change towards the sample surface, indicating that there are neither visible defects nor amorphous regions in the implanted area and below in the Ge substrate after PLM. This suggests that the $Ge_{1-x}Sn_x$ with 1.0 *at.* % Sn sample after PLM treatment at 0.5 J/cm² is a fully epitaxial, monocrystalline film, as shown by the high-resolution TEM image in the inset of Figure 4. This observation is in accordance with the RBS channeling results and indicates that the melted layer is deeper than the as-implanted layer and the regrowth of the sample after PLM is a bottom-up nanosecond-range liquid phase epitaxial process.

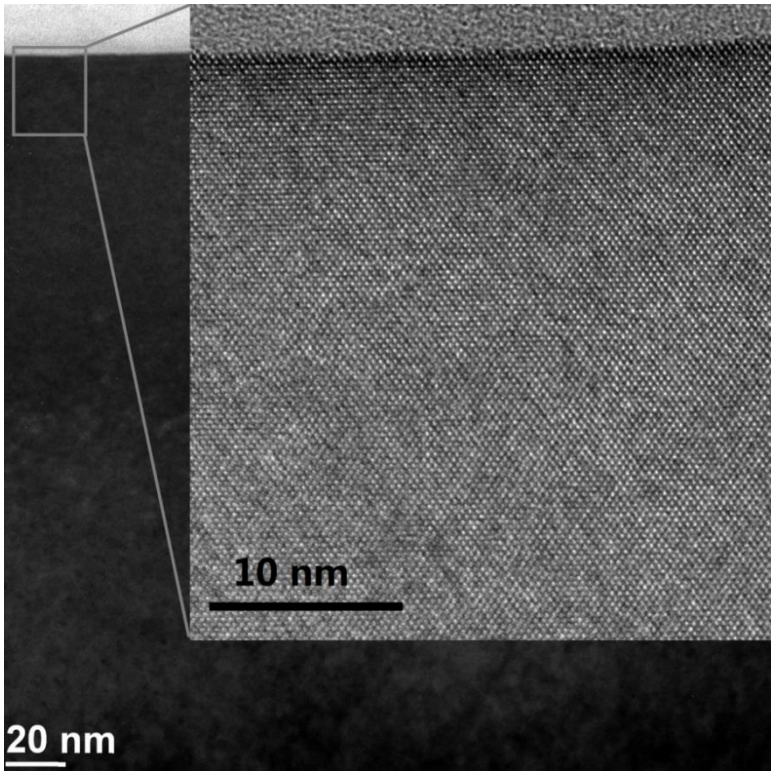

Figure 4.4 Cross-sectional bright-field TEM micrograph and high-resolution TEM image (inset) of $Ge_{1-x}Sn_x$ with 1 *at.* % Sn after PLM treatment.

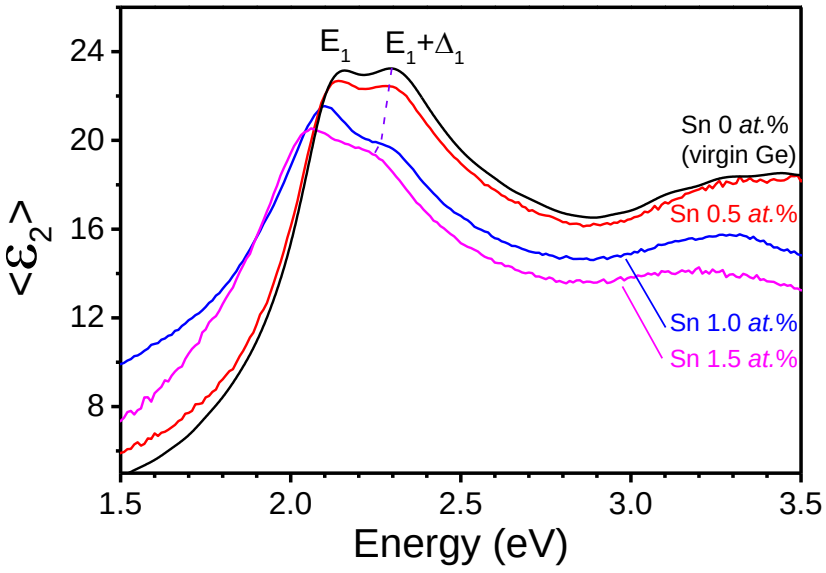

Figure 4.5 Imaginary parts (ε_2) of the complex dielectric function of PLM treated $Ge_{1-x}Sn_x$ alloys with various Sn concentrations (0 up to 1.5 *at.* %) determined by SE. The dashed line marks the shift of the $E_1+\Delta_1$ critical point.

The optical properties and the band structure evolution of the obtained $Ge_{1-x}Sn_x$ alloys were investigated by SE. Figure 4.5 shows the fitting results of the imaginary part ε_2 of the pseudodielectric function obtained from the $Ge_{1-x}Sn_x$ alloys with different Sn concentrations. Similar to the visible range Raman results discussed above, the influence of the Ge substrate can be excluded from the visible range ellipsometry presented here. Due to system limitations, the SE spectra were taken at the spectral range from 1 to 4 eV. Two peaks at about 2.1 and 2.4 eV corresponding to the E_1 and $E_1+\Delta_1$ critical points, respectively, are clearly resolved. These critical points describe transitions between the top two valence band and the lowest conduction band along the <111> direction in the Brillouin zone [36,77]. The clear redshifts of the critical points with increasing Sn concentration was observed. Even though the bandgap cannot be directly measured as the infrared range measurement is not available from our SE system, the redshifts of the E_1 and $E_1+\Delta_1$ with increasing Sn content provide a direct evidence of the bandgap shrinkage as a consequence of the Sn-doping [78], which is consistent with the structural analyses of the Sn-incorporation discussed above.

4.4 Conclusion

In this chapter, we present the epitaxial growth of monocrystalline $Ge_{1-x}Sn_x$ layers with Sn composition of up to 1.5 *at.* % achieved by ion implantation and PLM. The formation and the bandgap engineering of the monocrystalline $Ge_{1-x}Sn_x$ alloys were confirmed by various microstructural and optical investigations. Our results suggest a chip technology compatible route to prepare high quality $Ge_{1-x}Sn_x$ films with a wide tunability.

Chapter 5 $GaAs_{1-x}N_x$

Formation and photoluminescence of $GaAs_{1-x}N_x$ dilute nitride achieved by N-implantation and flash lamp annealing

5.1 Introduction

Nitrogen atom is an isoelectronic substituent for arsenic in GaAs. In virtue of its highly mismatched atomic size and electronegativity, a small amount of nitrogen substituting for arsenic in GaAs (i.e., $GaAs_{1-x}N_x$ dilute nitride) will lead to a pronounced bandgap shrinkage [10,15,54]. The bandgap decrease of GaAs is reported to be 120~180 meV per atomic percent of nitrogen substituted arsenic atoms at room temperature [10,15,17,53-56]. This effect makes N-doping a powerful method to modify the band structure of GaAs based materials for long wavelength optoelectronic devices [58]. Intensive efforts have been devoted to the theoretical [10,56] and experimental [10,15,53,54,79] study of $GaAs_{1-x}N_x$ for its distinctive structural and optical properties and potential applications. Band anticrossing (BAC) model has been developed to understand the band structure variation induced by N-doping in GaAs and the pressure and composition dependencies of the bandgap [10,55,79]. The BAC model is also applicable for some other highly mismatched alloys (HMAs, e.g., II-$VI_{1-x}O_x$, II-$VI_{1-x}S_x$) in which the substitutional anion is considerably different from the host anion [80-82].

However, it is a constant challenge to fabricate high quality $GaAs_{1-x}N_x$ due to the low solubility of N in GaAs. Molecular beam epitaxy [17,54] and metalorganic chemical vapour deposition [53] have been applied to synthesize $GaAs_{1-x}N_x$ dilute nitride with different N composition. Ion implantation is an

efficient method for the doping of N into GaAs beyond its equilibrium capacity. The amorphization induced by implantation will cause a downgrade of the optical and electrical properties of GaAs [83,84], which can be overcome by post-implantation annealing [70,85,86]. Since the binding energy of Ga-N is stronger than Ga-As, it is necessary to apply high energy to activate and incorporate N. However, high temperature furnace annealing (FA) or rapid thermal annealing (RTA) is not suitable for the treatment of GaAs based materials as GaAs tends to decompose and dilute N ions tend to evaporate when the annealing temperature is above 700 ºC. On the other hand, the nanosecond range pulsed laser melting (PLM) can achieve high enough temperature to melt the sample surface and activate the implanted nitrogen [85]. However, a large quantity of defects can be produced during the liquid phase epitaxy regrowth of $GaAs_{1-x}N_x$, which can reduce the carrier mobility of the materials and prevent the excitons from radiative recombination hence quenching the room temperature luminescence. Therefore, photoreflectance measurement is normally applied to analyze the bandstructure of $GaAs_{1-x}N_x$. The millisecond range FLA is applied in our work as a compromise between the ultra-short PLM and standard RTA or FA. The detailed description of FLA is given elsewhere [20,21]. Similar to PLM, only the surface of the samples can be heated up for several milliseconds. In our case of $GaAs_{1-x}N_x$, the annealing temperature of the sample surface was carefully controlled at about 100 °C below the melting point of the N-implanted GaAs layer in order to avoid defects being generated during liquid phase recrystallization. During FLA, the N atoms are incorporated onto the lattice site of As, thereby forming a $GaAs_{1-x}N_x$ dilute nitride layer on GaAs bulk substrate. Moreover, the millisecond range annealing time is long enough to anneal out most of defects generated during ion implantation process but simultaneously the time range of FLA is too short to activate the massive decomposition of GaAs during high temperature annealing.

In this paper, we present the synthesis of dilute nitride $GaAs_{1-x}N_x$ layer on GaAs wafer by N-implantation and FLA. Room temperature near bandgap photoluminescence (PL) from implantation-prepared $GaAs_{1-x}N_x$ is presented. The clear PL from our FLA treated $GaAs_{1-x}N_x$ indicates its good quality and high N-activation efficiency, which shows a promising potential for light emitting applications.

5.2 Experimental Setup

Semi-insulating (100) GaAs wafers were implanted at room temperature by nitrogen ions with the total fluences of 2.5×10^{15} and 5.0×10^{15} cm^{-2}. A double implantation with energies of 150 keV and 80 keV was applied in order to form a homogeneously nitrogen-doped layer of 200 nm thickness. According to the simulation by SRIM code [19], the two fluences correspond to an implanted N atomic concentration of x_{imp1}=0.38% and x_{imp2}=0.76%, respectively. Then, a 200 nm thick SiO_2 capping layer was deposited by PECVD at 200 °C in order to prevent the decomposition of GaAs and the evaporation of the implanted N during high-temperature FLA. To reform the lattice and to incorporate the N ions into GaAs, the as-implanted samples were processed by ultra-short FLA with a pulse duration of 3 ms. The surfaces were heated up to about 1100 °C during FLA and then cooled down also within milliseconds. Since the maximum surface temperature achieved during FLA is lower than the melting point of GaAs, the recrystallization of the implanted layer is a solid phase regrowth process. In order to estimate the optimized annealing conditions for the fabrication of the dilute nitride layer, some samples were annealed with a second flash under identical conditions. Between the two FLA, the samples were cooled down to room temperature sufficiently. After the FLA thermal treatment, the capping layer was removed by HF chemical etching. For comparison, the as-implanted sample was also treated by PLM with an energy

fluence of 0.34 J/cm^2 for 30 ns by a 308 nm XeCl laser and subsequent RTA at 950 °C for 10 s, which is the optimized condition for PLM with subsequent RTA reported by K.M. Yu *et al.* [70].

The structural properties of $GaAs_{1-x}N_x$ were investigated by micro-Raman spectroscopy. The Raman spectra were recorded in a backscattering geometry under a continuous 532 nm Nd:YAG laser excitation using a liquid-nitrogen-cooled charge coupled device. The optical properties of the $GaAs_{1-x}N_x$ samples were investigated by temperature-dependent PL spectroscopy. A continuous 532 nm Nd:YAG laser with an intensity of about 2 W/cm^2 was used to excite the $GaAs_{1-x}N_x$ layer at temperatures between 70 K and 300 K. The luminescence was dispersed by a Jobin Yvon Triax 550 monochromator and then recorded by a liquid-nitrogen-cooled InGaAs detector.

5.3 Results and discussion

Figure 5.1 shows the first-order micro-Raman spectra obtained from the flash lamp annealed $GaAs_{1-x}N_x$ layers, a virgin GaAs wafer, and the as-implanted sample for x_{imp1}=0.38%. According to the selection rules, the longitudinal optical (LO) phonon mode at about 292 cm^{-1} should be the only resolvable mode from the (100) oriented monocrystalline GaAs in the backscattering geometry. However, the transverse optical (TO) phonon mode located at about 267 cm^{-1}, which is theoretically forbidden, practically appears as a result of the disorder in the crystal structure. The disorder can be intrinsic or can be induced by highly mismatched ternary alloying. Therefore, the relative intensity between the LO and TO peak in the Raman spectra for different samples can be used as a fingerprint of the crystallinity of the samples.

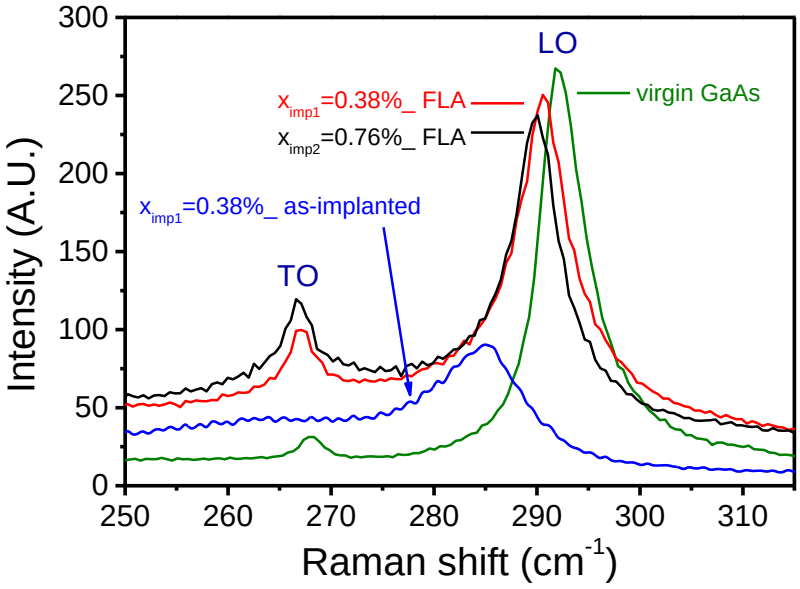

Figure 5.1 Raman spectra from FLA treated $GaAs_{1-x}N_x$ for x_{imp1}=0.38% and x_{imp2}=0.76% (marked as x_{imp1}=0.38%_FLA and x_{imp2}=0.76%_FLA, respectively). Raman spectra from the virgin GaAs and the as-implanted $GaAs_{1-x}N_x$ for x_{imp1}=0.38% are plotted for comparison.

The Raman spectrum obtained from the x_{imp1}=0.38% as-implanted sample shows two broad peaks at around 284 and 264 cm^{-1}, corresponding to the LO and TO phonon modes in amorphous GaAs, respectively. LO peaks dominate in the spectra from the FLA treated samples, peaking at 290.8 cm^{-1} and 289.9 cm^{-1}, for x_{imp1}=0.38% and x_{imp2}=0.76% samples, respectively. The appearance of the sharp LO mode after FLA suggests a recrystallization of the implantation induced amorphous layer. The LO peaks from N-doped GaAs samples have a slight but obvious shift to lower wavenumbers compared with virgin GaAs (291.7 cm^{-1}). In the meantime the TO mode shifts from 268.1 cm^{-1} of virgin GaAs to 267.1 cm^{-1} (x_{imp1}=0.38%) and 266.8 cm^{-1} (x_{imp2}=0.76%). The peak shift of the phonon modes has been reported as a consequence of N-incorporation into GaAs [87]. The x_{imp2}=0.76% sample exhibits a more significant shift, which indicates more N incorporation after FLA. The TO mode

from the annealed samples becomes stronger than that from the virgin sample, which is a typical behavior for ternary alloys [79].

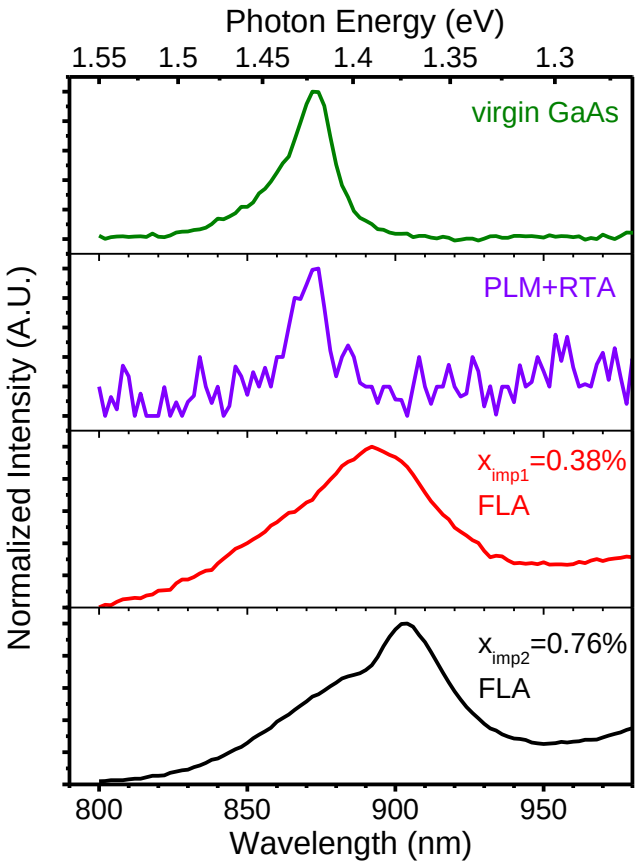

Figure 5.2 Room temperature PL spectra from the FLA treated $GaAs_{1-x}N_x$ samples for x_{imp1}=0.38% and x_{imp2}=0.76%, as well as the virgin GaAs and the PLM+RTA treated $GaAs_{1-x}N_x$ for comparison. The PL peaks from both FLA treated samples show a clear redshift compared with the PL from virgin GaAs. The spectra are normalized for better visibility of the peak positions. The intensities of the PL from FLA treated samples are plotted in Figure 3 and discussed in the following text.

Figure 5.2 displays the room temperature PL spectra from the $GaAs_{1-x}N_x$ samples. For the PLM+RTA treated sample, no obvious PL from $GaAs_{1-x}N_x$ can be detected. Only a weak PL peak at 873 nm (two orders of magnitude weaker than that from the virgin GaAs) from pure GaAs appears, which is

probably from the unimplanted GaAs beneath the $GaAs_{1-x}N_x$ layer. For the FLA treated x_{imp1}=0.38% sample, a distinct peak appears at around 893 nm (1.388 eV), while the near bandgap PL from the virgin GaAs wafer is observed at 873 nm (1.420 eV). Our previous research has shown that FLA process on virgin GaAs [88] or Ar-ion-implanted (not shown) GaAs will not cause a redshift of its near bandgap PL. Therefore, the redshift observed from N-implanted GaAs should be considered as a consequence of the N-incorporation. Here we assume that N-incorporation into GaAs would cause 170 meV bandgap shrinkage per atomic percent [15]. The bandgap reduction of 32 meV suggests an activated N concentration of x_{act1}=0.19% for x_{imp1}=0.38%, which implies that about 50% of implanted N atoms have been successfully incorporated into the lattice of GaAs during its recrystallization, i.e. the activation efficiency χ_1=50%.

With increasing nitrogen concentration, the PL peak of the FLA treated x_{imp2}=0.76% sample has a more pronounced redshift to 903 nm (1.373 eV). Consequently, the activated N concentration in $GaAs_{1-x}N_x$ is calculated to be x_{act2}=0.28% for x_{imp2}=0.76%, which suggests an activation efficiency of about χ_2=37%. In addition, an asymmetric broadening appears at the high energy side of the main PL peak, which can be attributed to the PL from the region beneath the box-like N-implanted layer, where the N concentration decreases drastically with deeper depth. As the PL from $GaAs_{1-x}N_x$ shifts more to the longer wavelength side for the higher doped (x_{imp2}=0.76%) sample, the PL contribution from the deeper region with a smaller N concentration appears as a shoulder. For the x_{imp1}=0.38% sample, the PL from deeper region with lower N concentration merges with the main PL from the implanted layer and cannot be distinguished.

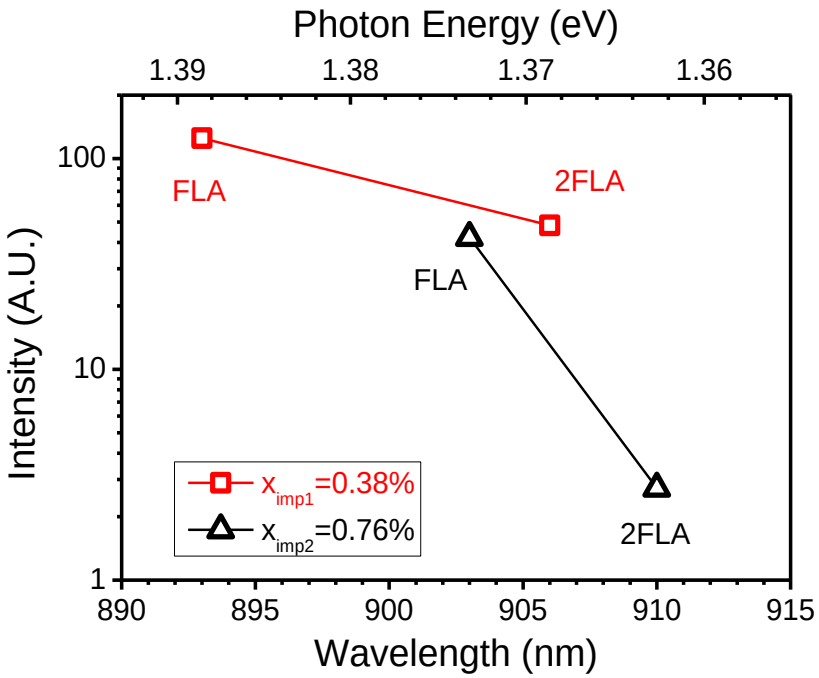

Figure 5.3 Variations of the PL peak positions and intensities for the $GaAs_{1-x}N_x$ samples with two N concentrations treated by single FLA (marked as FLA) and double FLA (marked as 2FLA).

A comparison of the room temperature PL peak positions and intensities for single and double flash annealed samples is depicted in Figure 3. After the second FLA, the near bandgap PL exhibits a further redshift to 906 nm (1.368 eV) for x_{imp1}=0.38%, and to 910 nm (1.363 eV) for x_{imp2}=0.76%, respectively, indicating that the second flash results in a higher activated N concentration. The incorporation efficiency is calculated as 80% for x_{imp1}=0.38% and 44% for x_{imp2}=0.76%, respectively. The intensity of the PL decreases after the second FLA, as a consequence of higher incorporation fraction of highly mismatched N composition and more disorder generated during annealing.

Temperature-dependent PL was performed in order to further verify the origin of the peak at 906 nm for the double flash treated $GaAs_{1-x}N_x$. Figure 4 shows the PL spectra of the sample measured at the temperatures ranging from 70 K to 300 K. At low temperatures the PL spectra consist of several peaks whose intensity strongly depends on the temperature. The intense

infrared PL peaks at around 1.22 μm and 1.30 μm are due to the radiative transitions from conductive band and arsenic vacancies to defect X-level in GaAs, respectively. The detailed study of the two peaks can be found in our previous work [23,88]. The feature at about 1.38 μm is attributed to the absorption of water in the light path of the PL system. In the high energy region of the PL spectrum at 70 K, two peaks located at 864 nm and 940 nm are well distinguishable. The broad band at 940 nm is due to the transition from the ionization level of As vacancy to the valence band, which is totally thermally quenched at temperatures above 180 K [89,90]. The high quenching rate and the insensitivity of the peak position of the 940 nm band with increasing temperature are typical behaviours for defect-like centers. On the other hand, the PL contribution at about 864 nm at 70 K shows a clear redshift to 906 nm at room temperature and lower quenching rate with increasing temperature. Such behaviour is similar to the bandgap PL from virgin GaAs. In addition, the temperature dependence of the peak position shift for $GaAs_{1-x}N_x$ is weaker than that for virgin GaAs as the temperature rises above 180 K. The nitrogen induced weakening of the temperature dependence of the bandgap PL peak position has been reported by A. Polimeni *et al.* [54]. Therefore, the temperature dependence of this PL peak confirms our assumption that the peak originates from the near-bandgap PL in $GaAs_{1-x}N_x$.

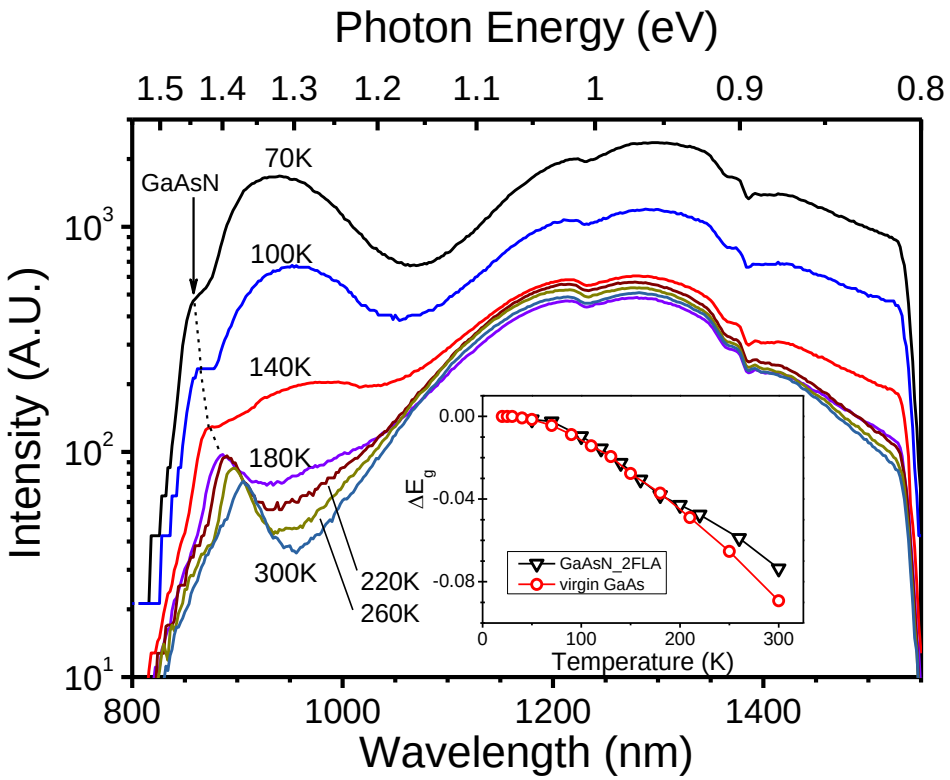

Figure 5.4 Temperature dependent PL of double FLA treated $GaAs_{1-x}N_x$ for x_{imp1}=0.38%. The intensities are plotted in logarithmic scale for better visibility. The shift of the near-bandgap PL from $GaAs_{1-x}N_x$ is marked by a dashed line. Inset shows the bandgap shrinkage (ΔE_g) of $GaAs_{1-x}N_x$ (marked as GaAsN-2FLA) with increasing temperature determined by the near-bandgap PL peak position, in comparison with a virgin GaAs sample. The cut-off from 1520 nm is due to the limit of the InGaAs detector.

5.4 Conclusion

In conclusion, we present the preparation of $GaAs_{1-x}N_x$ dilute nitride layer by nitrogen-ion implantation and FLA. Raman results indicate the recrystallization of the as-implanted amorphous GaAs:N layer. The appearance and the redshift of the room temperature near bandgap PL from $GaAs_{1-x}N_x$ confirm the formation of the high quality alloys with potential application in optoelectronics. Both ion implantation and post-implantation FLA

are standard processing techniques in IC-industry, which can be utilized for mass production. Therefore, the successful synthesis of $GaAs_{1-x}N_x$ dilute nitride material by ion implantation and FLA shows a promising prospect as a cost-effective solution to its applications.

Chapter 6 Defect engineering in GaAs

Origin and enhancement of the 1.3 μm luminescence from GaAs treated by ion implantation and flash lamp annealing

6.1 Introduction

GaAs and GaAs based materials are widely used in optoelectronic and photovoltaic devices for its direct bandgap as well as outstanding optical and electrical performances. At room temperature, GaAs has a bandgap of 1.42 eV which corresponds with 0.87 μm luminescence [91]. Many approaches have been designed on GaAs related matrices to achieve 1.30 μm and 1.55 μm emissions which are in the 2nd and 3rd transmission window of optical fibers. To achieve emissions at such wavelengths, one way is to modify the bandgap by alloying, i.e. to form ternary / quaternary alloys such as InGaAs / InGaAsP [92]. Another common method is to grow multiple quantum wells or quantum dots with GaAs and some other narrower bandgap materials (e.g., InAs), using quantum confinement to control the emission wavelength [60,93]. For practical applications, temperature insensitivity is one of the key indicators for the device performance. Besides these two approaches, proper defect engineering can also be used for the photoluminescence (PL) enhancement below the band gap of GaAs. The defect related luminescence bands in GaAs are in the spectral range of 0.8 – 1.35 eV, consisting of gallium and/or arsenic vacancy/interstitial complexes [61,62]. Related to the nature of a defect level, its luminescence can also be relatively immune to temperature changes. The origin of most defect related emission bands in GaAs is quite well established in literature except the 0.95 eV (1.30 μm) emission whose origin is still

controversial. Considering the fact that light at a wavelength of 1.30 μm traveling through quartz fiber suffers minimum attenuation, such a GaAs based light source could be applied in the field of optical fiber communications. For industrial production, the cost and the efficiency are two decisive factors. Ion implantation and post-implantation thermal annealing (e.g., rapid thermal annealing (RTA) [94] and flash lamp annealing (FLA)) [20] are compatible techniques in IC-industry. Therefore, to realize the 1.30 μm emission from GaAs-based materials by ion implantation and FLA is promising for its advantages of low-cost, high efficiency, and IC-compatibility.

In previous work [23] we have presented defect engineering in nitrogen-doped and undoped semi-insulating GaAs (SI-GaAs) wafers by millisecond range FLA for efficient room temperature 1.30 μm PL emission. According to the experimental results, the 1.30 μm PL observed from a FLA treated virgin GaAs wafer is due to radiative transitions between energy levels of intrinsic defects in GaAs, and this emission can be enhanced by nitrogen implantation followed by FLA [23]. In this paper we present a detailed study of the influence of N, P, In, and Zn implantation combined with FLA on the 1.30 μm PL emission from GaAs. Different doping types are used for comparison to investigate the origin of the 1.30 μm PL emission. Proper N-, P-, and In-doping leads to the formation of a GaAs based ternary alloy, among which N and P tend to occupy the As site while In goes to the Ga site, which will result in the significant differences on defect-type in GaAs. Zn-doping leads to the conduction type change in GaAs (i.e., from semi-insulating to p-type). Our results show that indium-doping has greatly enhanced the emission at 1.30 μm by more than two orders of magnitude compared with FLA treated virgin SI-GaAs. Moreover, the influence of the conductivity type on the luminescent properties of the GaAs wafers is also discussed. In the case of Zn-doping, the 1.30 μm emission is completely quenched, which is consistent with our previous results shown for p-type Mn-doping [23].

6.2 Experimental Setup

Semi-insulating (100) GaAs wafers were implanted at room temperature with N, P, In, and Zn ions. The dopants are implanted with different kinetic energies to ensure that the concentration depth profiles of the dopants are almost the same. Nitrogen ions are implanted deeper considering the diffusion of nitrogen during annealing. The as-implanted and virgin GaAs wafers were annealed by a flash lamp system at different energy densities (i.e., different annealing temperatures on surface) for 3 ms or 20 ms. The annealing energy density was controlled by changing the power supplied to the Xe lamps used during FLA. For the whole sample series, the optimized annealing condition for the 1.30 µm PL emission presented in this paper are slightly below the melting point of the virgin/as-implanted GaAs. The implantation and annealing parameters are given in Table 1. To prevent the decomposition of the GaAs surface and the evaporation of As during annealing, 200 nm thick SiO_2 layers were deposited on the surface of the GaAs wafers by PECVD at 200 °C before annealing, and then were chemically etched in HF:H_2O solution after annealing.

Optical properties of the virgin and annealed GaAs samples were investigated by temperature dependent PL. Micro-Raman spectroscopy was used to determine the structural properties of GaAs and the influence of doping before and after FLA. The PL measurements were performed using a 532 nm Nd:YAG laser with an intensity of about 3 W/cm^2 for sample excitation at temperatures from 20 K to 300 K. The PL signal was dispersed by a Jobin Yvon Triax 550 monochromator and recorded by a liquid-nitrogen-cooled InGaAs detector. The Raman spectra were collected in a backscattering geometry in the range of 150 to 600 cm^{-1} by a liquid-nitrogen-cooled charge coupled device with 532 nm Nd:YAG laser excitation.

Table 6.1 Sample preparation: fluence and kinetic energy for different ion implantations, flash lamp annealing time and energy densities for post-treatment.

Dopants		- (virgin)	N*		P	In	Zn
Ion implantation	Fluence (cm^{-2})	-	$2x10^{15}$	$8x10^{15}$	$2x10^{15}$	$2x10^{15}$	$2x10^{15}$
	Energy (keV)	-	30	70	40	140	120
	Doping range (nm)	-	250		90	90	100
	Peak concentration (at. %)	-	2		1.6	1.8	1.4
Flash lamp annealing	Time (ms)	20	3		20	20	20
	Optimized energy density (J/cm^2)	89	53		89	89	89

* Nitrogen was implanted deeper than other dopants due to its diffusion and evaporation during FLA. A double implantation (i.e., dopants are implanted with two different kinetic energies) was applied in order to form a thick and homogenous doping layer.

6.3 Results and Discussion

6.3.1 Photoluminescence

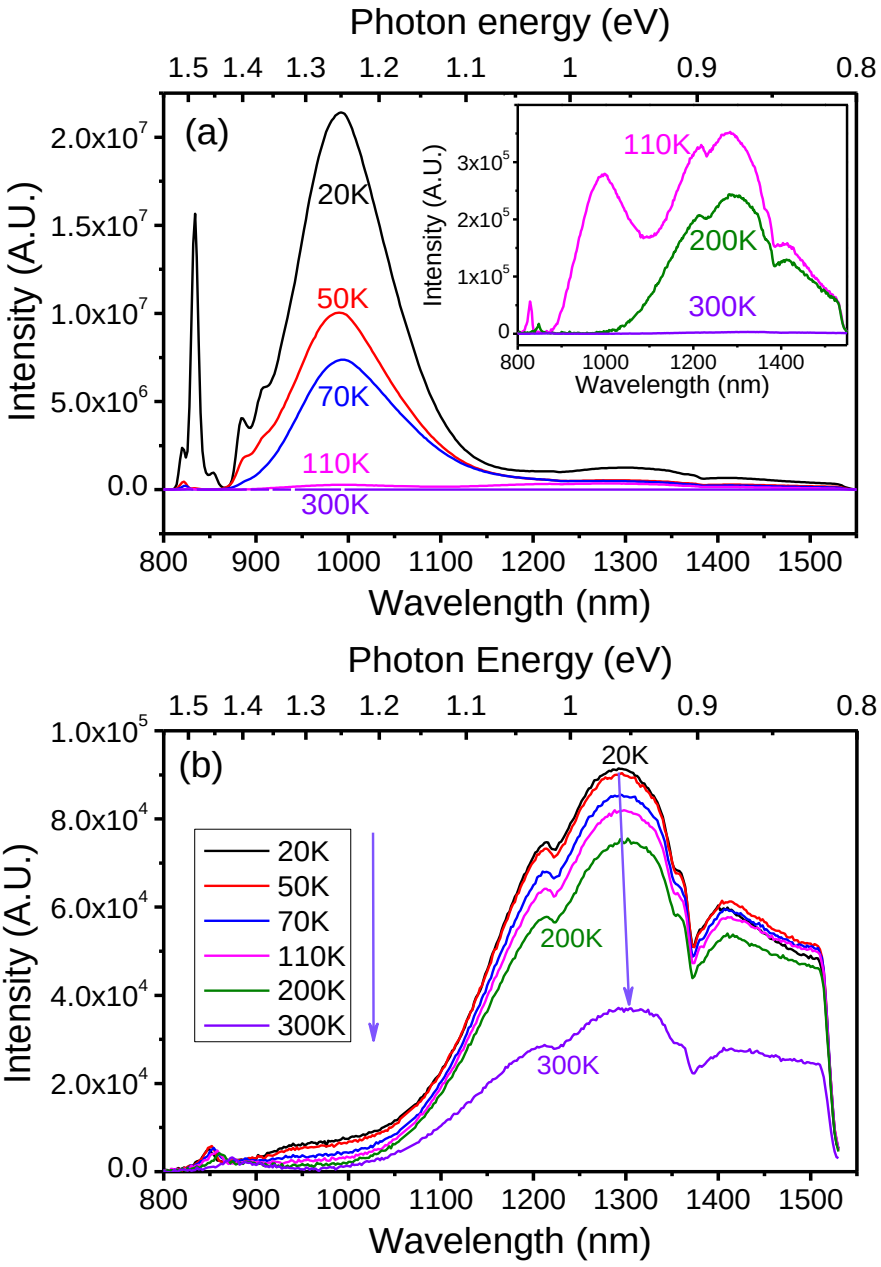

Figure 6.1 PL spectra of (a) virgin and (b) 20 ms flash lamp annealed (energy density 89 J/cm^2) SI-GaAs wafer for different temperatures as indicated. Inset of (a) shows the magnified PL spectra of virgin GaAs at 110 K, 200 K, and 300 K. The cut-off at around 1520 nm is due to the limit of the InGaAs detector.

Figure 6.1 (a) shows the temperature dependent PL spectra obtained from a virgin SI-GaAs wafer measured between 20 K to 300 K. The PL spectra are composed of several strongly temperature dependent peaks related to the near band edge emission (NBE) and defect centers in GaAs. The luminescence peak at 820 nm (at 20 K) shows a significant redshift and intensity decrease with increasing temperature, which is the typical behavior for the NBE. The peaks at 834 nm and 992 nm quench faster than the NBE peak, but no significant redshift is observed. The two PL peaks are assigned to transitions from the conduction band to energy levels of the carbon acceptor (C_{As}) and Ga vacancy (V_{Ga}), respectively [95-99]. Moreover, a broad peak at about 1.30 µm as well as an accompanying peak at 1.22 µm is observed at 20 K. The intensity of both peaks decreases with rising temperature. At 300 K, the two peaks almost vanish (three orders intensity decrease) due to the thermal quenching. In addition, the trough at about 1.38 µm that occurs in each spectrum is attributed to the absorption of water existing in the PL system.

After flash lamp annealing, the PL spectrum (see Figure 6.1 (b)) differs significantly from the spectrum of the non-annealed sample (Figure 1 a). Except for the two NIR emissions at around 1.30 µm and 1.22 µm, most of the PL peaks from the non-annealed sample either disappear or become much weaker compared with the virgin wafer. In contrast to the complete thermal quenching of the C_{As} and V_{Ga} defect-related luminescence, both NIR peaks at 1.22 and 1.30 µm become detectable at 300 K. Though the two peaks still maintain a decay trend as temperature increases, they show only 60% intensity decrease from 20 K to 300 K, which is remarkably different from the virgin sample before annealing. At the same time, the two NIR peaks show only 14 nm redshift.

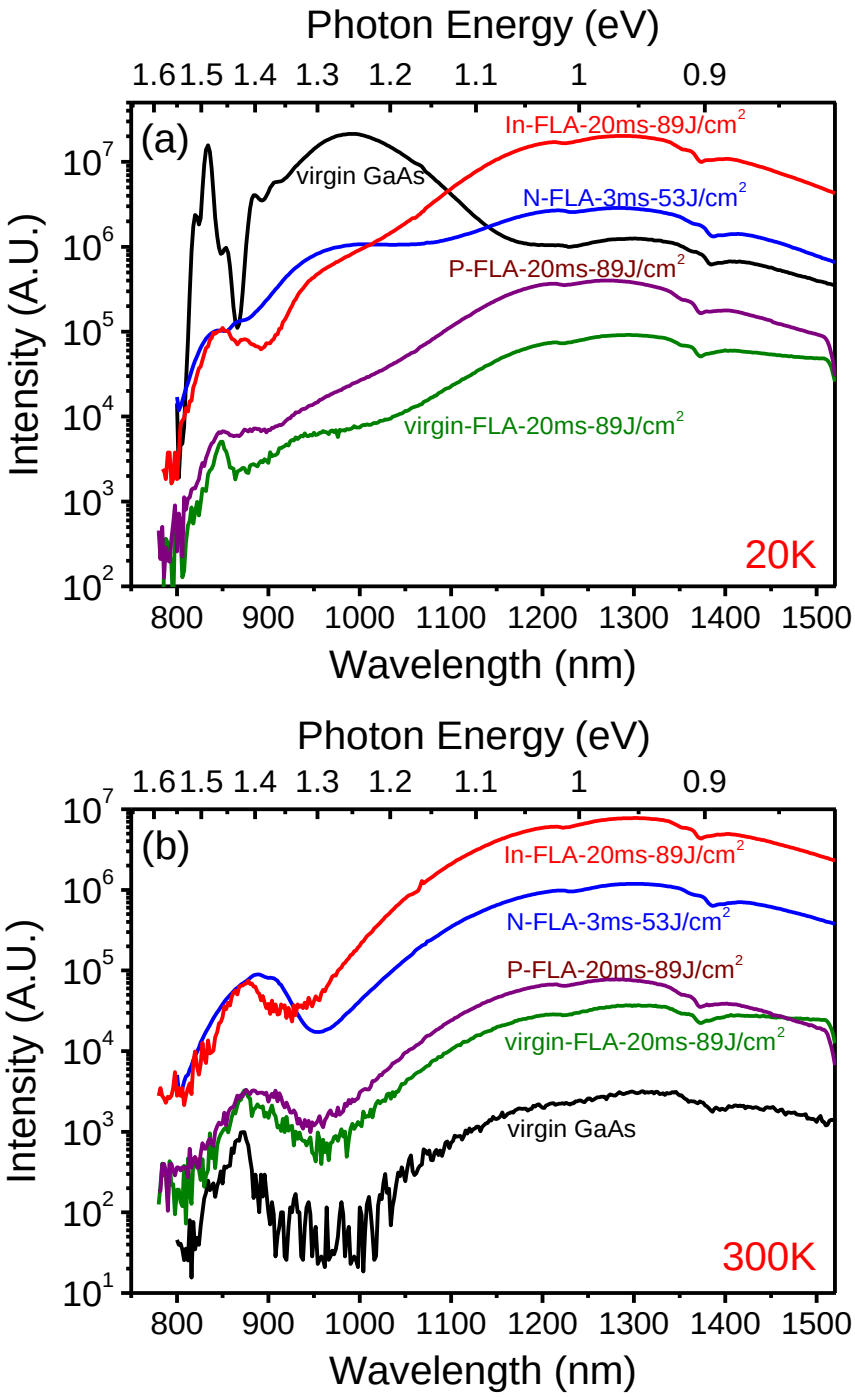

Figure 6.2 PL spectra measured at 20 K (a) and 300 K (b) from In-, P-, N-implanted GaAs treated by FLA. PL from the non-annealed virgin GaAs as well as the FLA treated virgin GaAs at 20 K and 300 K (plotted on linear scale in Figure 1 (a,b)) is shown for comparison. All spectra show the 1.30 μm emission accompanied by the 1.22 μm emission with a similar line shape but different intensities.

Figure 6.2 shows PL spectra from FLA-treated virgin, N-, P-, In- implanted GaAs as well as virgin GaAs wafer tested at 20 K (a) and 300 K (b). For the spectra at 300 K the PL line shapes for different samples are similar: the 1.30 μm peak accompanied by the 1.22 μm peak dominates, while a weaker NBE appears at around 875 nm.

For FLA treated N-implanted GaAs (marked as N-FLA-3ms-53J/cm^2) at 20 K, the PL peak at 842 nm weakens and redshifts as the temperature increases (not shown here), which can be attributed to the NBE from GaAs. The broad peak at about 0.99 μm can be attributed to emission from the transition between conduction band to Ga-vacancy (V_{Ga}), as shown and discussed for the virgin GaAs sample. For the 1.30 μm emission, the behavior is similar to the flash lamp annealed virgin GaAs shown in Figure 1(b), i.e., 60 % intensity reduction and 8 nm redshift from 20 K to 300 K.

At around 850 nm one PL peak is also detected at 20 K from FLA treated P-implanted GaAs (marked as P-FLA-20ms-89J/cm^2), corresponding to the NBE from GaAs. The emission from V_{Ga} for P-implanted GaAs is rather weak at all temperatures, which is the main difference from the annealed GaAs:N samples. The 1.30 μm emission shows stronger quenching in comparison to the virgin and N implanted sample. Between 20 K and 300 K the intensity decreases by 80% and shifts by 12 nm.

For the FLA treated GaAs:In sample (marked as In-FLA-20ms-89J/cm^2), the 1.30 μm emission is greatly enhanced (see Figure 6.2 and Figure 6.3). The alloying of 1.8 at. % of indium with GaAs can bring about no more than 26 meV bandgap shrinkage, which corresponds to 17 nm redshift of the NBE PL [100]. Therefore the 1.30 μm emission cannot originate from transitions between the conduction and valence band of InGaAs. The main difference between the incorporation of indium and group V elements into GaAs is that indium replaces gallium in the matrix, while group V elements substitute arsenic. The substitution of indium has been confirmed by Rutherford backscattering

channeling spectrometry (not shown). Therefore indium-doped GaAs differs from nitrogen- and phosphorus-doped GaAs in the type and the concentration of the defects. At 20 K we observed a very weak NBE peak at about 840 nm with the typical redshift for NBE emission as the temperature increases. In the spectra only the 1.30 µm emission accompanied by the 1.22 µm peak dominates. The V_{Ga} peak at about 0.99 µm appears as a shoulder. From 20 K to 300 K a 14 nm redshift and 60 % intensity decrease occur, which suggests good thermal stability of the 1.30 µm luminescence.

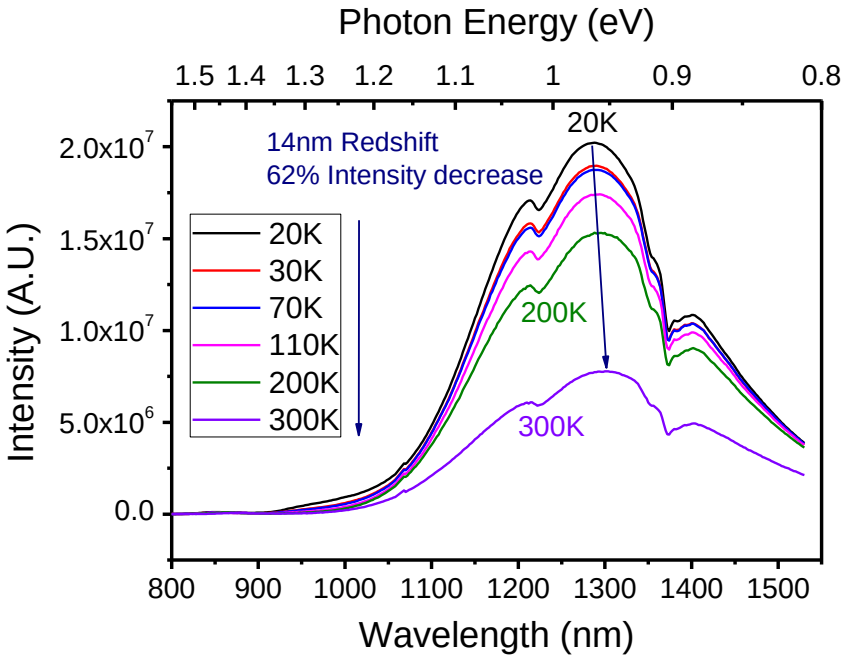

Figure 6.3 Temperature dependent PL spectra of indium-doped GaAs treated by flash lamp annealing for 20 ms at 89 J/cm^2. The 1.30 µm and 1.22 µm peaks dominate between 20 K and 300 K.

Figure 6.4 shows the intensity differences and the variation tendencies with increasing temperature of 1.30 µm emissions from different samples. As the temperature increases, all the samples show monotonic decrease in the emission intensity. The annealed virgin GaAs has the weakest 1.30 µm luminescence while the group-V implanted GaAs samples show an enhancement of this emission. Indium-doped GaAs exhibits the strongest 1.30

μm emission which is more than two orders of magnitude higher than that observed from the virgin GaAs. Compared with the thermal quenching of the 1.30 μm PL from the non-annealed virgin GaAs wafer (see Figure 1a), the FLA treated samples only show a limited intensity reduction. Therefore we conclude that FLA can induce the 1.30 μm luminescence at room temperature in virgin and implanted GaAs samples, i.e., stabilize such emission from temperature influence.

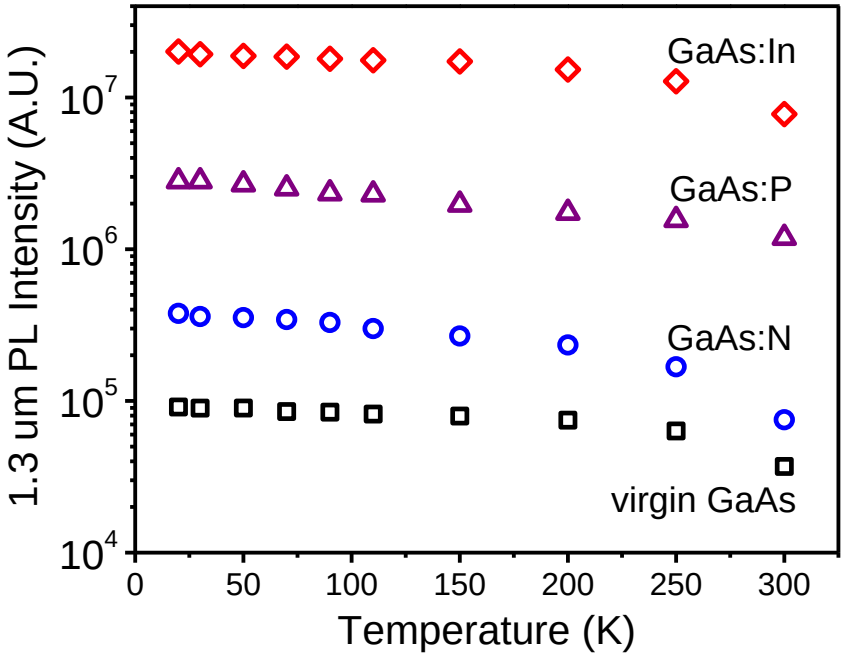

Figure 6.4 Intensities of the 1.30 μm PL emission from FLA-treated GaAs:In, GaAs:P, GaAs:N as well as virgin GaAs as the function of temperature. For a better view the vertical axis is in logarithmic scale.

It is also worth to note that for the virgin GaAs and GaAs implanted by P and In, a stronger 1.30 μm PL is observed from 20 ms FLA treated samples than from 3 ms FLA treated ones, whereas for N-implanted GaAs 3 ms annealing time is superior to 20 ms (not shown here). This is probably due to the instability of gaseous N and its low solubility in GaAs. During high-temperature FLA, N is easy to evaporate from the as-implanted wafer due

to its low solubility and high combination energy with gallium in GaAs. Therefore shorter annealing times introduce less negative effects for N-implanted GaAs.

6.3.2 Raman

The influence of doping and millisecond flash lamp annealing on the microstructure of GaAs was investigated by means of micro-Raman spectroscopy. Figure 5(a) shows the first-order micro-Raman spectra obtained from non-annealed and flash lamp annealed Indium-implanted GaAs. According to the selection rules in the backscattering geometry from the (100) oriented monocrystalline GaAs, the Raman spectra should reveal only the longitudinal optical (LO) phonon mode at 292 cm^{-1}, whereas the transverse optical (TO) phonon mode located at 268.6 cm^{-1} is forbidden.

The Raman spectrum obtained from the indium-as-implanted sample shows two broad peaks at 284 and 258 cm^{-1} corresponding to the LO and TO phonon modes in amorphous GaAs, respectively, due to the destruction of the top layer of the GaAs wafer during ion implantation. After FLA treatment, such two peaks shifted back to 291 and 267 cm^{-1}, close to the standard value of crystalline GaAs, which indicates the FLA-induced regrowth of the lattice. The appearance of the TO mode suggests that the annealed samples are not monocrystalline and contain defects. As the inset of Figure 6.5 (a) shows, the intensity of LO phonon mode decreases with rising annealing temperature, whereas the TO phonon mode becomes stronger. At the same time, the 1.30 µm PL intensity shows an upward-trend. By changing the annealing energy density from 84 J/cm^2 to 89 J/cm^2, the LO mode weakens and the TO mode strengthens to a great extent. Simultaneously, the intensity of 1.30 µm PL rises by three orders of magnitude. For the 89 J/cm^2 annealed sample, two weak peaks appear at around 255 and 200 cm^{-1}, which can be attributed to crystalline arsenic clusters [101]. This suggests that with higher annealing

temperature, decomposition has occurred to some extent in the near surface region.

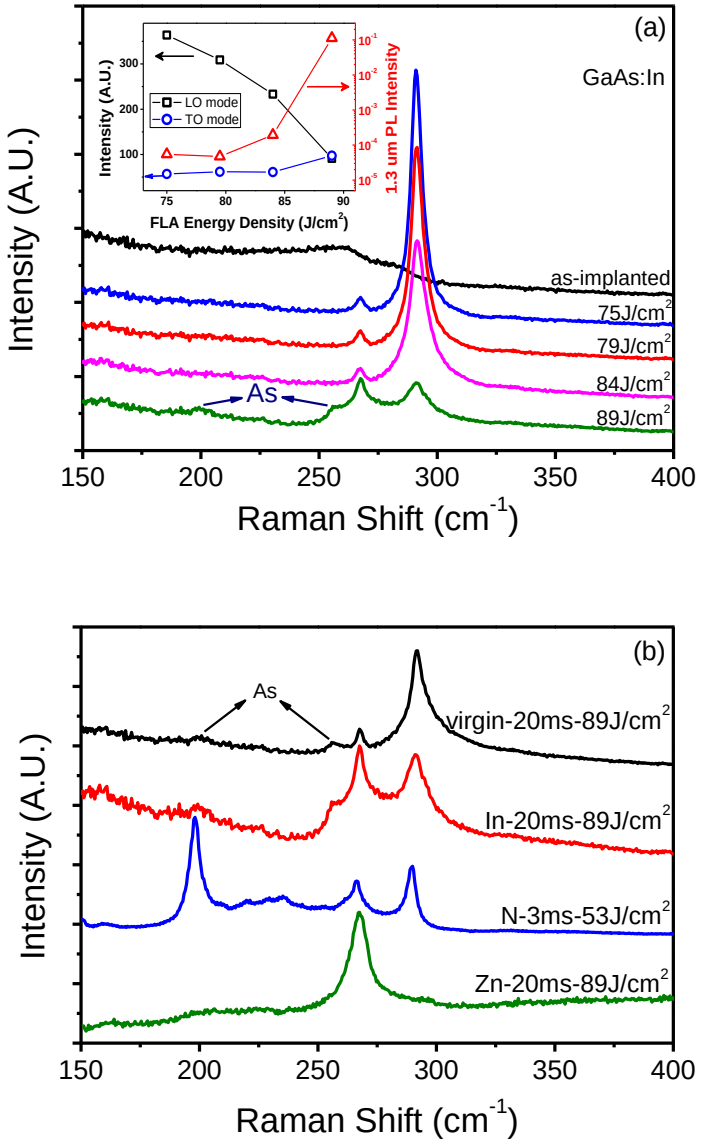

Figure 6.5 (a) Raman spectra from indium-implanted GaAs, both as-implanted and 20 ms flash lamp annealed at different energy densities are shown. The inset of (a) compares the intensity variations of the 1.3 μm PL and the LO and TO Raman modes with respect to different FLA energy densities. (b) Raman spectra of FLA treated virgin GaAs, GaAs:In, GaAs:N, GaAs:Zn, under which annealing condition the strongest 1.30 μm PL (for GaAs:Zn the strongest NBE) is observed. The spectra are vertically shifted for comparison.

Figure 6.5 (b) compares the Raman spectra from the samples exhibiting the 1.30 μm PL emission with optimized annealing condition. The Raman spectrum from Zn-doped GaAs, where the 1.30 μm PL quenches distinctly (see Figure 6), is shown for comparison. For the virgin GaAs annealed at 89 J/cm^2, the differences to the data obtained for 80 J/cm^2 shown in the previous work [23] are the appearance of the TO peak and two arsenic peaks. For N-doped GaAs, a strong peak appears at the position of 200 cm^{-1}, which is reported to be the longitudinal acoustic (LA) mode derived from N-induced alloy disorder [79]. Compared with the standard wavenumber of the LO mode for bulk GaAs, the peaks revealed a −2 cm^{-1} shift due to lattice shrinkage by N-doping [79,102]. For the Zn-doped p-type GaAs the LO phonon mode of GaAs is almost invisible, while the strongest peak can be attributed to the coupled-LO-phonon-plasmon mode (CLOPM) which is usually optically active in heavily doped p-type semiconductors [103]. According to the influence of hole concentration on the CLOPM peak shift [104], the hole concentration in our Zn-doped GaAs is of the order of 10^{19} cm^{-3}.

6.3.3 Origin of the 1.30 μm emission

In our previous paper [23], we have reviewed some discussions on the 1.30 μm (0.95 eV) emission from the literature. The temperature dependence of the 1.30 μm emission is the main difference between those results in the literature and ours. In our case, we observed the 1.30 μm emission from the virgin GaAs and GaAs implanted with various ions after FLA. Therefore, it is reasonable to conclude that the emission is due to defect centers in GaAs rather than the dopants. The excitation intensity dependence of the NBE and 1.30 lm PL spectra have been tested from the FLA treated GaAs:N at 20K (not shown). The NBE intensity exhibits a linear dependence on the excitation intensity, whereas the 1.30 lm PL intensity can be fitted to be proportional to

the square root of the excitation intensity. This square root dependence of the 1.30 lm emission is the typical behavior of the defect-related PL [105].

Moreover, we have observed a great enhancement of the 1.30 μm PL from indium-doped GaAs as compared to group-V doped GaAs and virgin GaAs. Note that indium-doping increases the total amount of the group-III sites and leads to an increase of the density of the arsenic vacancies (V_{As}), while the incorporation of group-V elements does not have such an effect. In addition, for all GaAs samples implanted with different dopant species, the highest 1.30 μm emissions always appear at the samples treated at the highest annealing energy density (i.e. approaching the melting point) in each temperature series. The crystalline arsenic peaks can only be found from the corresponding Raman spectra of these samples. Taking all these into consideration, the 1.30 μm emission should be closely related with V_{As}.

For further investigations we implanted Zn into the SI-GaAs wafer, then the sample was treated by FLA for 20 ms with the energy density of 89 J/cm^2. In addition, N was also doped into a commercial p-type (Zn-doped) GaAs wafer under the same implantation and FLA conditions for N-doping in SI-GaAs listed in Table 1. The PL spectra of the two samples are shown in Figure 6, marked as GaAs:Zn, p-GaAs:N, respectively. Zn-implantation leads to heavy p-type doping, which is totally different from the group III or V doping. The results show that such heavy p-type doping completely quenches the 1.30 μm PL. The absence of the 1.30 μm emission at a p-GaAs:N sample also corroborates this conclusion. From these facts we conclude that p-type doping has negative influence on the 1.30 μm PL. Therefore the defects related to 1.30 μm PL should be n-type or neutral.

We also investigated the processed GaAs samples which exhibit 1.30 μm PL emission by positron annihilation spectroscopy (PAS). Results indicate the existence of V_{As}-X defects in those samples which exhibit 1.30 μm PL [148(9-SP)]. Considering the fact that the defects detectable by PAS have to

be either neutral or negatively charged, while the V_{As} are always positively charged, p-type doping can suppress the recombination of carriers between levels of V_{As} and X by positively charging the X-centers. Based on the discussion on V_{As} and X, and considering that the arsenic vacancies form shallow donor levels located at about 30, 60, or 140 meV below the conduction band and they are positively charged (V_{As}^{n+}) while the X defects' level is located at about 0.5 eV above the valence band [9], the transition between the V_{As}-donor and X-acceptor pairs can give rise to the 1.30 μm emission. The recombination of electrons and holes between the conduction band and X-acceptor level generates the 1.22 μm emission which always accompanies the main 1.30 μm emission in our samples.

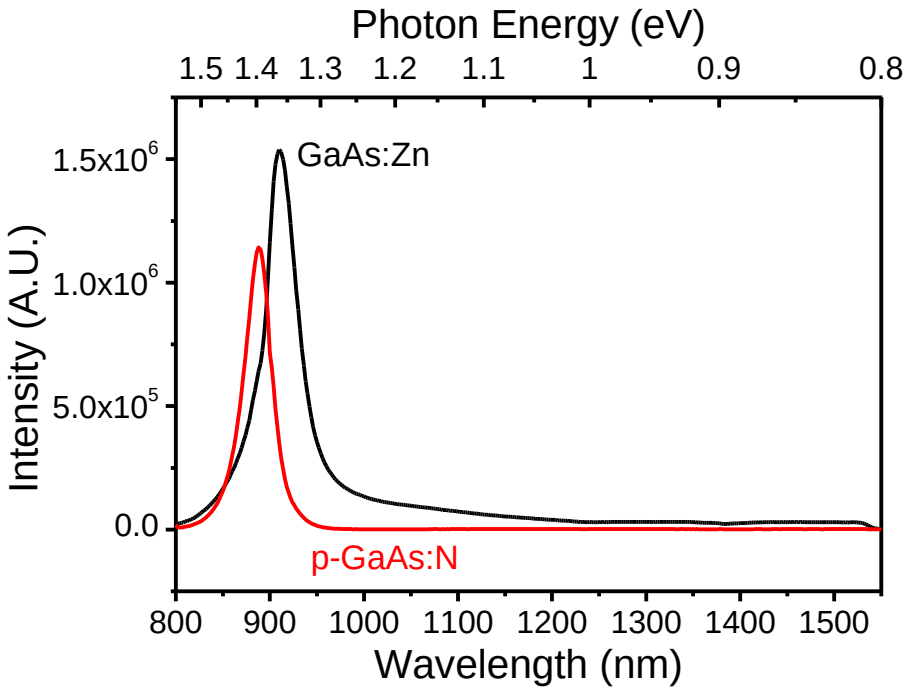

Figure 6.6 Room temperature PL spectra of FLA treated GaAs:Zn and p-GaAs:N. The 1.30 μm emission is absent from these two samples.

6.4 Conclusion

In summary, we have presented temperature stable 1.30 μm PL emission from FLA treated undoped and doped GaAs. The highest intensity of such emission was obtained from indium-doped GaAs, and is more than two orders of magnitude higher than that from the virgin sample. The origin of this temperature stable 1.30 μm emission is related to a transition between V_{As}-X defect complexes. Being generated from defect levels affords the 1.30 μm emission outstanding thermal stability with respect to the emitted wavelength and intensity. Considering the fact that ion implantation followed by flash lamp annealing is a very convenient and efficient method in industry of chip fabrication and can be easily applied to large scale production, FLA treated GaAs can be a promising candidate for optical-fiber communication devices, especially for those applied in some extreme conditions.

Chapter 7 Conclusions and future trends

This thesis presents the syntheses of two kinds of HMAs (i.e., $Ge_{1-x}Sn_x$, $GaAs_{1-x}N_x$) by ion implantation and ultrashort annealing. Detailed investigations and discussions on the structural and optical properties of $Ge_{1-x}Sn_x$ and $GaAs_{1-x}N_x$ are presented.

Various experimental techniques, Raman spectroscopy, XRD, RBS channeling spectroscopy, and TEM, have been applied to characterize the structural properties. The recrystallization of the implantation-induced amorphized layer and the incorporation of the dopants after short time annealing have been confirmed. The bandgap engineering by highly mismatched doping have been verified by optical measurements (SE for $Ge_{1-x}Sn_x$, PL for $GaAs_{1-x}N_x$).

7.1 Comparison of PLM and FLA applied to highly mismatched doping

The advantages of ultra-short annealing techniques in the non-equilibrium doping have been introduced and experimentally verified in this thesis. PLM and FLA, both of which are considered as ultra-short annealing techniques, work in different regimes. Therefore, PLM and FLA are applicable to different materials or different surface temperatures.

As discussed in Chapter 4, the Sn-implanted Ge layer has been completely amorphized, and the recrystallization of this amorphized layer is a bottom-up liquid phase regrowth process. Our experiments (Raman, RBS, and TEM) have shown that FLA below the melting point of the surface layer can also recrystallize the amorphized layer. However, the reformed structure after being heated up by FLA is polycrystalline according to the RBS channeling and TEM measurements (not shown). The results suggest that the recrystallization is a simultaneous process within the heated layer as a

consequence of the relatively long time heating and smooth temperature gradient from the surface to the deeper region. On the contrary, the temperature gradient generated by PLM are much sharper compared with that generated by FLA because of the shorter annealing time. Therefore, the recrystallization takes place from the solid-liquid interface. In our case, the melting depth is deeper than the amorphized layer, so that the crystalline structure at the interface acts as a template and promotes the monocrystalline epitaxial regrowth from liquid phase.

GaAs, as a compound semiconductor, contains various kinds of defects, e.g., unintentional dopants, Ga / As interstitials, vacancies, antisites, and theirs complexes. These defects will be massively generated during re-solidification process from liquid phase after annealing, which can induce a critical downgrade of the crystallinity and the optoelectronic properties of the material. In addition, GaAs tends to decompose at temperature higher than 700 ºC, hence forming Ga / As clusters. Some of the As atoms can evaporate from the material. The high power fluence of the ns-range pulsed excimer laser and the strong absorption of the laser beam from the material (Ge and GaAs) suggest that the near-surface region will definitely be melted during irradiation. Due to these facts, PLM is not suitable for the improvement of GaAs based materials. As shown in chapter 6, the near band-edge PL was completely quenched from PLM treated $GaAs_{1-x}N_x$ sample. On the other hand, the N ions for doping are of much smaller atomic mass compared with that of Ga and As atoms in the matrices, therefore the required implantation energy for N to reach a certain depth is not so high. In contrast with Sn doping into Ge, relatively low energy implantation of ions with smaller mass will not cause the complete destruction of the matrices, but will only bring about an increase of the amount of the defects and the downgrade of the crystallinity. Therefore, the aim of the annealing in this case is to improve the quality of the structure rather than to reconstruct the whole structure. In this case, the bottom-up liquid phase

regrowth is not necessary. The annealing temperature of the millisecond FLA can be well controlled by changing the charge voltage of the capacitors, so that the implantation-induced partially amorphized layer can be heated up to the temperature approaching but not reaching the melting point to increase the efficiency of incorporation. In addition, a capping layer such as SiO_2 or SiC, which is transparent to the flash light, can be deposited on the surface of the samples that need to be annealed, in order to prevent the decomposition and accelerate the cooling process of the top layer. Our investigation suggests an efficient doping for N in GaAs by high temperature FLA induced solid phase regrowth.

7.2 Suggestions on future work

7.2.1 PLM with longer wavelength and shorter time

As introduced in this thesis, PLM has been proved to be an effective solution to the non-equilibrium synthesis of $Ge_{1-x}Sn_x$ alloys. However, the applicable Sn concentration in monocrystalline $Ge_{1-x}Sn_x$ alloys synthesized by ion implantation and PLM cannot reach as high as that achieved by MBE. As discussed above, the penetration depth of a 308 nm XeCl laser in Ge is less than 20 nm whereas the implanted depth is about 100 nm. The melting of the deeper region is mainly due to thermal conduction. Therefore, a complete melting of the amorphized Sn doped Ge layer requires a higher temperature on the surface, which can decelerate the cooling and recrystallization. Moreover, a higher concentration of Sn will bring about a distinct reduction of the melting point because of the extreme low melting point of Sn (~232 °C) and the low phase-transition-temperature of α-Sn (13.5 °C) [46]. Consequently, Sn atoms beyond the solubility can be segregated during the relatively long cooling down process, especially for a high Sn concentration doping, as

discussed in ref. [46]. To avoid the segregation and the overheating on the surface, a laser with longer wavelength but shorter pulse duration can be a solution. A frequency-doubled pulsed Nd:YAG laser or Nd:Glass laser, which can emit light with a wavelength of 532 nm, can be a candidate to meet the requirements. The penetration depth of 532 nm light in Ge is about 40 nm according to the absorption coefficient [64], therefore the surface overheating should be much less than that for the 308 nm excimer laser. The typical pulse duration of a Nd:YAG laser is 5 ns, shorter than the excimer laser. Consequently, the segregation of the supersaturating Sn dopant can probably be suppressed. For a Nd:Glass laser, the gain medium can be grown to a large size to generate a large laser spot, which is promising for mass production. Moreover, the Nd:YAG and Nd:Glass lasers are solid state lasers, which are of lower cost and have a better stability and a longer lifetime than the excimer gas lasers. The combination of ion implantation and solid state laser annealing can be a cost-effective solution for the mass production of $Ge_{1-x}Sn_x$ alloys.

7.2.2 Co-implantation in Ge to approach direct bandgap

As introduced in Chapter 2, n-type doping is another approach to achieve direct bandgap Ge. The energy difference between the Γ band and the L band has been reduced by Sn-doping. Further approach to direct bandgap can be done by n-type doping. In this case, we can apply a combined implantation of Sn and n-type dopant such as P or As into Ge within the same range, and then use PLM to activate the dopants simultaneously. The As doping in Ge by implantation and PLM has been reported as an efficient solution for heavy n-type doping [47].

In addition, tensile strain is also proved to be an effective solution to approach direct bandgap for Ge based materials. PLM is proved to be a strain-conserving method according to the results of X-ray diffraction (XRD) reciprocal space mapping (RSM) (see Chapter 4), In our case, the $Ge_{1-x}Sn_x$ monocrystalline layer is determined to be compressively strained on Ge

substrate, as the lattice parameter of $Ge_{1-x}Sn_x$ is larger than that of the Ge substrate. Si, which can be easily alloyed with Ge, has a smaller lattice constant than Ge and Sn. Therefore, Si can be co-implanted with Sn to shrink the lattice to a certain value smaller than Ge, hence introducing a tensile strain between the alloy and the Ge substrate.

The dopants introduced above (i.e., P, As, and Si) all have smaller atomic mass than Sn. The interaction of ion and solid for Sn should be much stronger than the others. In addition, their solubility in Ge is also higher than that for Sn. Therefore, the co-implantation of Sn and other dopants introduced above to achieve Ge based direct bandgap materials should be applicable.

7.2.3 Combination of FLA and other annealing techniques for dilute nitride $GaAs_{1-x}N_x$

Our investigation has shown a decreasing N incorporation efficiency with increasing concentration of the implanted N. For a higher implantation concentration, the absolute amount of the incorporated N is proved to be increased with the optimized FLA treatment. However, the increment of the incorporated N is not proportional to the increment of the implanted N. More implanted N remains in the interstitial positions as defects, which will cause a critical downgrade of the crystallinity hence quenching the room temperature PL. Therefore, the sample with higher N concentration exhibits a weaker PL intensity, as shown in Chapter 5.

K.M. Yu *et al.* have reported a N activation efficiency of 50% by PLM and RTA for 1.8 *at.* % of implanted N in GaAs, whereas the efficiency achieved by RTA is only 10% - 15%. This suggests that a higher temperature up to the melting point of GaAs generated by PLM is beneficial to the high efficiency incorporation of N. The following RTA treatment is applied to reduce the amount of defects and improve the crystallinity. Due to the weak thermal stability of GaAs and $GaAs_{1-x}N_x$, RTA with applicable temperature and duration is not efficient enough to anneal out most of the defects generated during

implantation and / or PLM thereby realizing room temperature PL (see Chapter 5). In this case, to replace RTA with FLA, i.e. the combination of PLM and FLA, can probably be an effective approach for the efficient incorporation of N into GaAs. FLA, which is applied to anneal out the defects in GaAs generated from implantation, is probably also effective for those defects generated from PLM induced liquid phase recrystallization. If so, this method can be utilized to prepare $GaAs_{1-x}N_x$ with a higher N concentration of good quality to realize room temperature PL, which would be a giant leap to its application. The idea of combining different ultrashort annealing techniques would provide more possibilities for the non-equilibrium syntheses of HMAs and many other materials.

References

1. Claudio Ferrari, Claudio Bocchi, Characterization of Semiconductor Heterostructures and Nanostructures, Chapter 4: Strain and composition determination in semiconducting heterostructures by high-resolution X-ray diffraction, (Elsevier, 2008).
2. J. A. Van Vechten and T. K. Bergstresser, Phys. Rev. B 1, 3351 (1970).
3. J. Wu, W. Walukiewicz, and E. E. Haller, Phys. Rev. B 65, 233210 (2002).
4. Kirstin McLean Alberi, Valence Band Anticrossing in Highly Mismatched Alloys, PhD thesis (2008).
5. I. Vurgaftman, J. R. Meyer, and L. R. Ram-Mohan, J. Appl. Phys. 89, 5815 (2001).
6. Shigeki Sakai and Takuo Sugano, J. Appl. Phys. 50, 4143 (1979).
7. M. Bugajski, A. M. Kontkiewicz, and H. Mariette, Phys. Rev. B 28, 7105 (1983).
8. J. Wu, W. Shan, and W. Walukiewicz, Semicond. Sci. Technol. 17, 860 (2002).
9. Y.J. Huo, PhD Thesis, Strained Ge and GeSn band engineering for Si photonic integrated circuits, (2010).
10. W. Shan, W. Walukiewicz, J. W. Ager, III, E. E. Haller, J. F. Geisz, D. J. Friedman, J. M. Olson, and S. R. Kurtz, Phys. Rev. Lett. 82, 1221 (1999).
11. W. Shan, W. Walukiewicz, K. M. Yu, J. Wu, J. W. Ager III, E. E. Haller, H. P. Xin, and C. W. Tu, Appl. Phys. Lett. 76, 3251 (2000).
12. W. Shan, W. Walukiewicz, J. W. Ager III, K. M. Yu, J. Wu, E. E. Haller, Y. Nabetani, T. Mukawa, Y. Ito, and T. Matsumoto, Appl. Phys. Lett. 83, 299 (2003).
13. K. M. Yu, W. Walukiewicz, W. Shan, J. Wu, J. W. Beeman, M. A. Scarpulla, O. D. Dubon, and P. Becla, J. Appl. Phys. 95, 6232 (2004).
14. W. Shan, K. M. Yu, W. Walukiewicz, J. W. Beeman, J. Wu, J. W. Ager III, M. A. Scarpulla, O. D. Dubon and E. E. Haller, Appl. Phys. Lett. 84, 924 (2004).
15. J.D. Perkins, A. Mascarenhas, Y. Zhang, J.F. Geisz, D.J. Driedman, J.M. Olson, and S. R. Kurtz, Phys. Rev. Lett. 82, 3312 (1999).

16. W. Smith and J. Hashemi, Foundations of Materials Science and Engineering, 4th ed. (New York: McGraw-Hill, 2006).
17. S. Francoeur, G. Sivaraman, Y. Qiu, S. Nikishin, and H. Temkin, Appl. Phys. Lett. 72, 1857 (1998).
18. R. Ragan and H. A. Atwater, Appl. Phys. Lett. 77, 3418 (2000).
19. J. F. Ziegler, Nucl. Instru. and Methods in Phys. Res. B 219–220, 1027 (2004).
20. W. Skorupa, T. Gebel, R. A. Yankov, S. Paul, W. Lerch, D. F. Downey, and E. A. Arevalo, J. Electrochem. Soc. 152, G436 (2005).
21. S. Prucnal, T. Schumann, W. Skorupa, B. Abendroth, K. Krockert, and H.J. Möller, Acta Physica Polonica A, 120(1), 30 (2011).
22. J. M. Poate, in C. W. White and P. S. Peercy (eds.), Laser and Electron Beam Processing of Materials, Academic Press, New York, 1980, p. 691.
23. S. Prucnal, Kun Gao, W. Anwand, M. Helm, W. Skorupa, and Shengqiang Zhou, Optics Express 20, 26075 (2012).
24. Jifeng Liu, Xiaochen Sun, Dong Pan, Xiaoxin Wang, Lionel C. Kimerling, Thomas L. Koch, and Jurgen Michel, Opt. Express, 15, 11272 (2007).
25. Physics of Group IV Elements and III–V Compounds, edited by O. Madelung, Landolt-Börnstein: Numerical Data and Functional Relationships in Science and Technology (Springer, Berlin, 1982), vol. 17a.
26. R. Roucka, J. Mathews, R. T. Beeler, J. Tolle, J. Kouvetakis, and J. Menéndez, Appl. Phys. Lett. 98, 061109 (2011).
27. M. J. Adams and P. T. Landsberg, Proceedings of the Ninth International Conference on the Physics of Semiconductors, Moscow (Akademiya Nauk) 1968, p. 619.
28. Y. Ishikawa, K. Wada, D. D. Cannon, J. F. Liu, H. C. Luan and L. C. Kimerling, Appl. Phys. Lett. 82, 2044 (2003).
29. C. G. Van de Walle, Phys. Rev. B 39, 1871 (1989).
30. Suyog Gupta, Germanium-Tin (GeSn) Technology, PhD Thesis (2013).
31. K. Alberi, J. Blacksberg, L. D. Bell, S. Nikzad, K. M. Yu, O. D. Dubon, and W. Walukiewicz, Phys. Rev. B 77, 073202 (2008).
32. W. J. Yin, X. G. Gong, and S.H. Wei, Phys. Rev. B 78, 161203(R) (2008).

33. J. Mathews, R. T. Beeler, J. Tolle, C. Xu, R. Roucka, J. Kouvetakis, and J. Menéndez, Appl. Phys. Lett. 97, 221912 (2010).
34. G. He and H.A. Atwater, Phys. Rev. Lett. 79, 1937 (1997).
35. Robert Chen, Hai Lin, Yijie Huo, Charles Hitzman, Theodore I. Kamins, and James S. Harris, Appl. Phys. Lett. 99, 181125 (2011).
36. Vijay R. D'Costa, Candi S. Cook, A. G. Birdwell, Chris L. Littler, Michael Canonico, Stefan Zollner, John Kouvetakis, and José Menéndez, Phys. Rev. B 73, 125207 (2006).
37. V. R. D'Costa, Y.-Y. Fang, J. Tolle, J. Kouvetakis, and J. Menéndez, Thin Solid Films 518(9), 2531 (2010).
38. O. Nakatsuka, N. Tsutsui, Y. Shimura, S. Takeuchi, A. and S. Zaima, Jpn. J. Appl. Phys. 49 04DA10 (2010).
39. H. Pérez Ladrón de Guevara, A. G. Rodríguez, H. Navarro-Contreras, and M. A. Vidal, Appl. Phys. Lett. 83, 4942 (2003)
40. J. Kouvetakis J. Menéndez, and A.V.G. Chizmeshya, Annu. Rev. Mater. Res. 36, 497 (2006).
41. S. Stefanov, J.C. Conde, A. Benedetti, C. Serra, J. Werner, M. Oehme, J. Schulze, D. Buca, B. Holländer, S. Mantl, and S. Chiussi, Appl. Phys. Lett., 100, 104101 (2012).
42. H. Pérez Ladrón de Guevara, A. G. Rodríguez, H. Navarro-Contreras, and M. A. Vidal, Appl. Phys. Lett. 84, 4532 (2004).
43. H. Lin, R. Chen, W. Lu, Y. Huo, T. I. Kamins, J. S. Harris, Appl. Phys. Lett. 100, 141908 (2012).
44. V. R. D'Costa, Y.-Y. Fang, J. Tolle, J. Kouvetakis, and J. Menéndez, Phys. Rev. Lett. 102, 107403 (2009).
45. S. Oguz, William Paul, T. F. Deutsch, B-Y. Tsaur, and D. V. Murphy, Appl. Phys. Lett. 43, 848 (1983).
46. A. Bhatia, W.M. Hlaing Oo, G. Siegel, P.R. Stone, K.M. Yu, and M.A. Scarpulla, J. Electron. Mater. 41, 837 (2012).
47. R. Milazzo, E. Napolitani, G. Impellizzeri, G. Fisicaro, S. Boninelli, M. Cuscunà, D. De Salvador, M. Mastromatteo, M. Italia, A. La Magna, G. Fortunato, F. Priolo, V. Privitera, and A. Carnera, J. Appl. Phys. 115, 053501 (2014).

48. M. Oehme, J. Werner, M. Gollhofer, M. Schmid, M. Kaschel, E. Kasper, and J. Schulze, IEEE Photonics Tech. Lett. 23(23), 1751 (2011).
49. W. Shan, K. M. Yu, W. Walukiewicz, J. Wu, J. W. Ager III, and E. E. Haller, J. Phys.: Condens Matter, 16 S3355 (2004).
50. K. Uesugi, I. Suemune, T. Hasegawa, T. Akutagawa, and T. Nakamura, Appl. Phys. Lett. 76, 1285 (2000).
51. L. Malikova, F. H. Pollak, RAJ Bhat, J. Electron. Mater. 27, 484 (1998).
52. R Bhata, C Caneaua, Lourdes Salamanca-Ribab, W Bic, and C Tu, J. Cryst. Growth, 195, 427 (1998).
53. M. Weyers, M. Sato, and H. Ando, Jpn. J. Appl. Phys. 31, L853 (1992).
54. A. Polimeni, M. Bissiri, A. Augieri, G. Baldassarri Höger von Högersthal, M. Capizzi, D. Gollub, M. Fischer, M. Reinhardt, and A. Forchel, Phys. Rev. B, 65, 235325 (2002).
55. S. Sakai, Y. Ueta, and Y. Terauchi, Jpn. J. Appl. Lett. 32, 4413 (1993).
56. W.G. Bi and C. W. Tu, Appl. Phys. Lett. 70, 1608 (1997).
57. Steven R. Kurtz, A. A. Allerman, E. D. Jones, J. M. Gee, J. J. Banas, and B. E. Hammons, Appl. Phys. Lett. 74, 729 (1999).
58. M. Kondow, T. Kitatani, S. Nakatsuka, M.C. Larson, K. Nakahara, Y. Yazawa, M. Okai, and K. Uomi, IEEE J. Sel. Top. Quantum Electron. 3, 719 (1997).
59. X. J. Wang, I. A. Buyanova, F. Zhao, D. Lagarde, A. Balocchi, X. Marie, C.W. Tu, J. C. Harmand, and W. M. Chen, Nat. Mater. 8, 198 (2009).
60. M. Grundmann, O. Stier, and D. Bimberg, Phys. Rev. B Condens. Matter 52, 11969 (1995).
61. C. V. Reddy, S. Fung, and C. D. Beling, Phys. Rev. B Condens. Matter 54(16), 11290 (1996).
62. H. Lei, H. S. Leipner, V. Bondarenko, and J. Schreiber, J. Phys. Condens. Matter 16(2), S279 (2004).
63. S. Zhou, PhD Thesis, Transition metal implanted ZnO: a correlation between structure and magnetism (2008).
64. D. E. Aspnes and A. A. Studna, Phys. Rev. B 27, 985 (1983).
65. T. Kim, M. R. Pillai, M. J. Aziz, M. A. Scarpulla, O. D. Dubon, K. M. Yu, J. W. Beeman, and M. C. Ridgway, J. Appl. Phys. 108, 013508 (2010).

66. R.F. Wood, C.W. White, and R.T. Young, Pulsed Laser Processing of Semiconductors (Orlando, FL: Academic, 1984).
67. C. D. Thurmond, F.A. Trumbore, and M. Kowalchik, J. Chem. Phys. 25, 799 (1956).
68. B. Vincent, F. Gencarelli, H. Bender, C. Merckling, B. Douhard, D. H. Petersen, O. Hansen, H. H. Henrichsen, J. Meersschaut, W. Vandervorst, M. Heyns, R. Loo, and M. Caymax, Appl. Phys. Lett. 99, 152103 (2011).
69. M. Kurosawa, N. Taoka, H. Ikenoue, O. Nakatsuka, and S. Zaima, Appl. Phys. Lett. 104, 061901, (2014).
70. K.M. Yu, W. Walukiewicz, M. A. Scarpulla, O. D. Dubon, J. Wu, J. Jasinski, Z. Liliental-Weber, J. W. Beeman, M. R. Pillai, and M. J. Aziz, J. Appl. Phys. 94, 1043 (2003).
71. M. A. Scarpulla, Oscar D. Dubon, K. M. Yu, O. Monteiro, M. R. Pillai, M. J. Aziz, and M. C. Ridgway, Appl. Phys. Lett. 82, 1251 (2003).
72. K. M. Yu, W. Walukiewicz, J. Wu, W. Shan, J. W. Beeman, M. A. Scarpulla, O. D. Dubon, and P. Becla, Phys. Rev. Lett. 91, 246403 (2003).
73. L. C. Feldman, J. W. Mayer, and S. T. Picraux, Materials Analysis by Ion Channeling (Academic Press, 1982).
74. H. Lin, R. Chen, Y. Huo, T. I. Kamins, and James S. Harris, Appl. Phys. Lett. 98, 261917 (2011).
75. M. Chu, Y. Sun, U. Aghoram, and S. E. Thompson, Annu. Rev. Mater. Res. 39, 203 (2009).
76. J. F. Schetzina and J. P. McKelvey, Phys. Rev. 181, 1191 (1969).
77. L. Viña, S. Logothetidis, and M. Cardona, Phys. Rev. B 30, 1979 (1984).
78. E. Kasper, M. Kittler, M. Oehme, and T. Arguirov, Photon. Res. 1, 69 (2013).
79. M.J. Seong, and H.M. Cheong, J. Korean Phys. Soc. 45, 217 (2004).
80. Y. C. Lin, H. L. Chung, W. C. Chou, W. K. Chen, W. H. Chang, C. Y. Chen, and J. I. Chyi, Appl. Phys. Lett. 97, 041909 (2010).
81. W. Walukiewicz, W. Shan, K. M. Yu, J. W. Ager, III, E. E. Haller, I. Miotkowski, M. J. Seong, H. Alawadhi, and A. K. Ramdas, Phys. Rev. Lett. 85, 1552 (2000).

82. K. M. Yu, W. Walukiewicz, J. Wu, J. W. Beeman, J. W. Ager III, E. E. Haller, I. Miotkowski, A. K. Ramdas and P. Becla, Appl. Phys. Lett. 80, 1571 (2002).
83. D. S. Dhaka, N. V. Tkachenko, H. L. E.-M. Pavelescu, M. Guina, A. Tukiainen, J. Konttinen, M. Pessa, K. Arstila, J. Keinonen, and K. Nordlund, Semicond. Sci. Technol. 21, 661 (2006).
84. C. Björkas, K. Nordlund, K. Arstila, J. Keinonen, V. D. S. Dhaka, and M. Pessa, J. Appl. Phys. 100, 053516 (2006).
85. K. M. Yu, W. Walukiewicz, J. W. Beeman, M. A. Scarpulla, O. D. Dubon, M. R. Pillai, and M. J. Aziz, Appl. Phys. Lett. 80, 3958 (2002).
86. K. M. Yu, Semicond. Sci. Technol. 17 785 (2002).
87. A. Mascarenhas and M. J. Seong, Semicond. Sci. and Tech. 17, 823 (2002).
88. Kun Gao, S. Prucnal, W. Skorupa, M. Helm and Shengqiang Zhou, J. Appl. Phys. 114, 093511 (2013).
89. J. C. Bourgoin, H. J. von Bardeleben, and D. Stiévenard, J. Appl. Phys. 64, R65 (1988).
90. S. Kuisma, K. Saarinen, P. Hautojarvi, C. Corbel, and C. LeBerre, Phys. Rev. B 61, 17 (1992).
91. I. Vurgaftman, J. R. Meyer, and L. R. Ram-Mohan, J. Appl. Phys. 89, 5815 (2001).
92. P. Sundgren, R. Marcks von Wurtemberg, J. Berggren, M. Hammar, M. Ghisoni, V; Oscarsson, E. Odling, and J. Malmquist, Electron. Lett. 39, 1128 (2003).
93. H. Y. Liu, I. R. Sellers, T. J. Badcock, D. J. Mowbray, M. S. Skolnick, K. M. Groom, M. Gutiérrez, M. Hopkinson, J. S. Ng, J. P. R. David, and R. Beanland, Appl. Phys. Lett. **85**, 704 (2004).
94. C. Y. Wong, Y. Komem, and H. B. Harrison, Appl. Phys. Lett. 50, 146 (1987).
95. S. Zemon, S. K. Shastry, P. Norris, C. Jagannath, and G. Lambert, Solid State Commun. **58**, 457 (1986).
96. K. Kuriyama, K. Yokoyama, K. Tomizawa, T. Takeuchi, and Hirokazu Takahashi, Appl. Phys. Lett. **61**, 17 (1992).

97. J. Garrido, J. L. Castaiio, J. Piqueras, and V. Alcober, J. Appl. Phys. **57**, 2186 (1985).
98. D. W. Kisker, H. Tews, and W. Rehm, J. Appl. Phys. **54**, 1332 (1983).
99. I. Ohbu, M. Takahama, and K. Hiruma, Appl. Phys. Lett. 61, 1679 (1992).
100. J. P. Laurenti, P. Roentgen, K. Wolter, K. Seibert, and H. Kurz, Phys. Rev. B 37, 4155 (1988).
101. J. Sapriel, Y.I. Nissim, B. Joukoff, J.L. Oudar, S. Abrahamr, and R. Beserman, J. Phys. (Paris). **45**, C5-75 (1984)
102. T. Prokofyeva, T. Sauncy, M. Seon, M. Holtz, Y. Qiu, S. Nikishin, and H. Temkin, Appl. Phys. Lett. 73, 1409 (1998).
103. M. R. Islam, N. F. Chen, and M. Yamada, Cryst. Res. Technol. 44, 215 (2009).
104. G. Irmer, M. Wenzel, and J. Monecke, Phys. Rev. B 56, 9524 (1997).
105. T. Schmidt, K. Lischka, and W. Zulehner, Phys. Rev. B 45, 8989 (1992).

Versicherung

Hiermit versichere ich, dass ich die vorliegende Arbeit ohne unzulässige Hilfe Dritter und ohne Benutzung anderer als der angegebenen Hilfsmittel angefertigt habe; die aus fremden Quellen direkt oder indirekt übernommenen Gedanken sind als solche kenntlich gemacht. Die Arbeit wurde bisher weder im Inland noch im Ausland in gleicher oder ähnlicher Form einer anderen Prüfungsbehörde vorgelegt. Die vorliegende Arbeit wurde am Helmholtz-Zentrum Dresden-Rossendorf in dem Institut für Ionenstrahlphysik und Materialforschung angefertigt und von Prof. Dr. Manfred Helm betreut. Ich erkenne die Promotionsordnung der Fakultät Mathematik und Naturwissenschaften der Technischen Universität Dresden vom 23.02.2011 sowie deren Änderung vom 09.07.2014 an.

Dresden, 19.12.2014

Gao, Kun　高昆